ACCSCIENCE PUBLISHING

International Journal of Bioprinting

RESEARCH ARTICLE

3D-printed Mg-substituted hydroxyapatite/gelatin methacryloyl hydrogels encapsulated with PDA@DOX particles for bone tumor therapy and bone tissue regeneration

Shangsi Chen[1†], Yue Wang[1,2†], Junzhi Li[3†], Haoran Sun[4*], Ming-Fung Francis Siu[2*], and Shenglong Tan[5*]

[1]Department of Mechanical Engineering, Faculty of Engineering, The University of Hong Kong, Pokfulam Road, Hong Kong, China

[2]Department of Building and Real Estate, Faculty of Construction and Environment, The Hong Kong Polytechnic University, Hung Hom, Kowloon, Hong Kong, China

[3]Department of Surgery, School of Clinical Medicine, The University of Hong Kong, Pokfulam Road, Hong Kong, China

[4]Koln 3D Technology (Medical) Limited, Hong Kong Science Park, Shatin, Hong Kong, China

[5]Department of Endodontics, Stomatological Hospital, Southern Medical University, Guangzhou, China

(This article belongs to the *Special Issue: Advanced Biomaterials for 3D Printing and Healthcare Application*)

Abstract

The development of bifunctional scaffolds for clinical applications, aimed at preventing tumor recurrence and promoting bone tissue regeneration simultaneously at the surgical site, is imperative in repairing bone tumor-related defects. In the current study, Mg-substituted hydroxyapatite (MgHAp) nanocomposites were synthesized via a biomineralization process. Doxorubicin hydrochloride (DOX), an anticancer drug, was incorporated in polydopamine (PDA) particles to synthesize PDA@DOX particles. MgHAp/gelatin methacryloyl (GelMA) hydrogels encapsulated with PDA@DOX particles were designed and fabricated to construct MgHAp/GelMA-PDA@DOX hydrogels via 3D printing. The 3D-printed MgHAp/GelMA-PDA@DOX hydrogels exhibited antitumor synergy by providing combined chemotherapy and phototherapy for bone tumor cell ablation. The hydrogels showed a good photothermal effect and could induce hyperthermia upon irradiation with an 808 nm near-infrared (NIR) laser. Moreover, MgHAp/GelMA-PDA@DOX hydrogels could release DOX sustainably and controllably. *In vitro* experiments demonstrated that 3D-printed MgHAp/GelMA-PDA@DOX hydrogels could effectively eradicate MG63 cells through the synergy of induced hyperthermia and DOX release. Furthermore, due to the sustained release of Mg^{2+}, 3D-printed MgHAp/GelMA-PDA@DOX hydrogels could promote the proliferation of rat bone marrow-derived mesenchymal stem cells and facilitate alkaline phosphatase activity and the expression of osteogenic genes, such as osteocalcin (*Ocn*), type I collagen (*Col1*), runt-related transcription factor-2 (*Runx2*), and bone morphogenetic protein-2 (*Bmp2*), indicating their excellent osteogenic effect. As a result, 3D-printed MgHAp/GelMA-PDA@DOX hydrogels showed great potential in the treatment of bone tumor-related defects by effectively killing tumor cells and simultaneously promoting bone tissue regeneration.

[†]These authors contributed equally to this work.

***Corresponding authors:**
Haoran Sun
(haoran@koln3d-tech.com)

Ming-Fung Francis Siu
(francis.siu@polyu.edu.hk)

Shenglong Tan
(tansl1989@outlook.com)

Citation: Chen S, Wang Y, Li J, Sun H, Siu MF, Tan S. 3D-printed Mg-substituted hydroxyapatite/gelatin methacryloyl hydrogels encapsulated with PDA@DOX particles for bone tumor therapy and bone tissue regeneration. *Int J Bioprint*. 2024;10(5):3526. doi: 10.36922/ijb.3526

Received: April 29, 2024
Accepted: May 14, 2024
Published Online: July 17, 2024

***Keywords*:** 3D printing; Magnesium; Anti-tumor effect; Bone tissue regeneration; Controlled release

1. Introduction

Osteosarcoma, a malignant bone tumor, is typically managed through surgical resection in clinical practice.[1] However, incomplete removal of tumor cells often leads to tumor recurrence. Consequently, chemotherapy and radiotherapy are commonly employed post-surgery to eradicate residual tumor cells.[2,3] Nevertheless, previous studies have indicated that these non-targeted approaches may result in side effects such as damage to normal cells and drug resistance development. To overcome these limitations, the development of an on-site controlled drug release system mediated and assisted by photothermal therapy (PTT) is crucial for minimizing drug dosage and avoiding cytotoxicity while enhancing therapeutic efficacy in tumor treatment.[4,5] Photothermal agents play an essential role in achieving effective PTT by inducing hyperthermia at cancerous site and simultaneously modulating drug release upon near-infrared (NIR) laser irradiation, thereby effectively eradicating residual tumor cells and enhancing antitumor efficacy.[6,7] Among various photothermal agents, such as gold nanoparticles, copper nanoparticles, magnetic iron-oxide nanoparticles, and carbon-based nanomaterials, polydopamine (PDA) nanoparticles have attracted significant interest in tissue engineering and controlled drug release due to their remarkable biocompatibility, biodegradability, and excellent photothermal property.[8,9] Furthermore, the abundant catechol and amine groups of PDA nanoparticles confer excellent adhesive capability that facilitates high drug loading efficiency. In this context, many studies have employed PDA nanoparticles for encapsulating diverse drugs and biomolecules in tissue engineering and cancer therapy applications.[10,11]

Resection of a bone tumor inevitably results in bone defects post-surgery. Despite the inherent self-regeneration ability of native bone tissue, three-dimensional (3D) tissue engineering scaffolds are preferred to be used to significantly accelerate the healing process of bone defects.[12,13] Tissue engineering scaffolds possess 3D structures that mimic the anatomical characteristics and provide essential functions of targeted tissues through the combination of suitable biomaterials and cells, along with the incorporation of appropriate biomolecules, and therefore have been widely used for treating bone defects.[14–16] Compared to conventional 3D scaffold manufacturing technologies, i.e., solvent casting/particle leaching, freeze-drying, gas forming, thermal-induced phasing separation, and electrospinning, 3D printing technology significantly enhances the potential in regenerating tissues due to its remarkable ability in constructing customized and patient-specific scaffolds that closely mimic the intricate and complex anatomical structures of native tissues.[17–19] Numerous 3D-printed scaffolds have been extensively designed and employed to repair bone tissues in preclinical and clinical trials. For example, some 3D-printed metallic scaffolds (e.g., stainless steel, titanium) have been used in clinical practice for bone tissue engineering.[20] Among various 3D-printed scaffolds, gelatin methacryloyl (GelMA)-based hydrogels and hydroxyapatite (HAp)-based scaffolds have shown great potential in bone tissue engineering.[21–23]

GelMA is a popular biomaterial for 3D printing.[24,25] It is an engineered gelatin-based biomaterial synthesized through the methacrylation of the lysine groups in the gelatin backbones.[26] As a result, GelMA exhibits great similarity to gelatin in terms of excellent biocompatibility, biodegradability, and temperature-responsive behavior, as well as the presence of Arg-Gly-Asp (RGD) sequences, which facilitate cell adhesion. Additionally, GelMA possesses good photo-crosslinking ability and can be covalently crosslinked with water-soluble photoinitiators when exposed to visible or ultraviolet (UV) light, thereby forming stable hydrogel networks. Therefore, 3D-printed GelMA hydrogels have gained significant attention in bone tissue engineering.[27,28] For example, Zhang et al. demonstrated that 3D-printed reduced graphene oxide (rGO)/GelMA hydrogels could enhance osteogenic and neurogenic dual differentiation simultaneously for potential neutralized bone regeneration.[29] However, it should be noted that GelMA inks often exhibit poor printability and the resulting GelMA hydrogels possess inadequate mechanical strength, posing challenges for 3D printing and bone tissue regeneration.

Many efforts have been devoted to improving the printability of GelMA inks and enhancing the mechanical performance of 3D-printed GelMA hydrogels.[25,30] Generally, incorporating ceramic nanoparticles in GelMA hydrogels has proven effective in addressing these challenges.[31,32] HAp—a bioceramic known for its exceptional biocompatibility, bioactivity, and osteoconductivity—is widely used as a bone substitute biomaterial, and HAp-based scaffolds have demonstrated significant potential in bone tissue regeneration. Previous studies have indicated that 3D-printed HAp/GelMA hydrogels could improve the printability of inks, enhance mechanical strength, and promote bone tissue regeneration.[33] For example, Song et al. demonstrated

that HAp/GelMA hydrogels showed excellent mechanical strength and could facilitate osteogenic differentiation *in vitro* and accelerate the formation of new bone in rabbit skull defects *in vivo*.[34] Furthermore, previous studies have revealed that magnesium (Mg)-doped HAp (MgHAp) displayed a superior osteogenic effect in comparison to HAp, owing to the sustained release of Mg^{2+} ions. The release of Mg^{2+} enabled to modulate bone metabolism, regulate osteoblast and osteoclast activity, and stimulate new bone formation.[35,36] Consequently, compared to HAp/GelMA hydrogels, 3D-printed MgHAp/GelMA hydrogels may potentially provide an enhanced therapeutic efficacy for the treatment of bone defects.

In the current study, to build an on-site controlled drug release system that can induce hyperthermia and modulate drug release for eradicating tumor cells and simultaneously promote bone tissue regeneration, MgHAp/GelMA hydrogels encapsulated with PDA@DOX particles (MgHAp/GelMA-PDA@DOX) were fabricated via 3D printing (Figure 1). PDA particles encapsulated with an anticancer drug, doxorubicin hydrochloride (DOX), were synthesized and then incorporated in MgHAp/GelMA hydrogels. The incorporation of MgHAp significantly improved the printability of inks and enhanced the mechanical strength of resulting hydrogels. Moreover, 3D-printed MgHAp/GelMA-PDA@DOX hydrogels exhibited a good photothermal effect and enabled sustainable and controllable release of DOX. *In vitro* experiments demonstrated that 3D-printed MgHAp/GelMA-PDA@DOX hydrogels could be combined with chemotherapy and PTT and hence effectively eradicate MG63 osteosarcoma cells. Compared to HAp/GelMA-PDA hydrogels, MgHAp/GelMA-PDA hydrogels promoted proliferation and osteogenic differentiation of rat bone marrow-derived mesenchymal stem cells (rBMSCs) *in vitro* owing to the sustained release of Mg^{2+}. Therefore, 3D-printed MgHAp/GelMA-PDA@DOX hydrogels hold great potential for both cancer therapy and bone tissue regeneration, which is desirable for the treatment of bone tumor-related defects.

2. Materials and methods

2.1. Materials

Type I collagen (COL1), citric acid, gelatin (Gel; type A from porcine skin, powder, gel strength ~300 g Bloom), methacrylic anhydride (MA; 94%), 2-hydroxy-

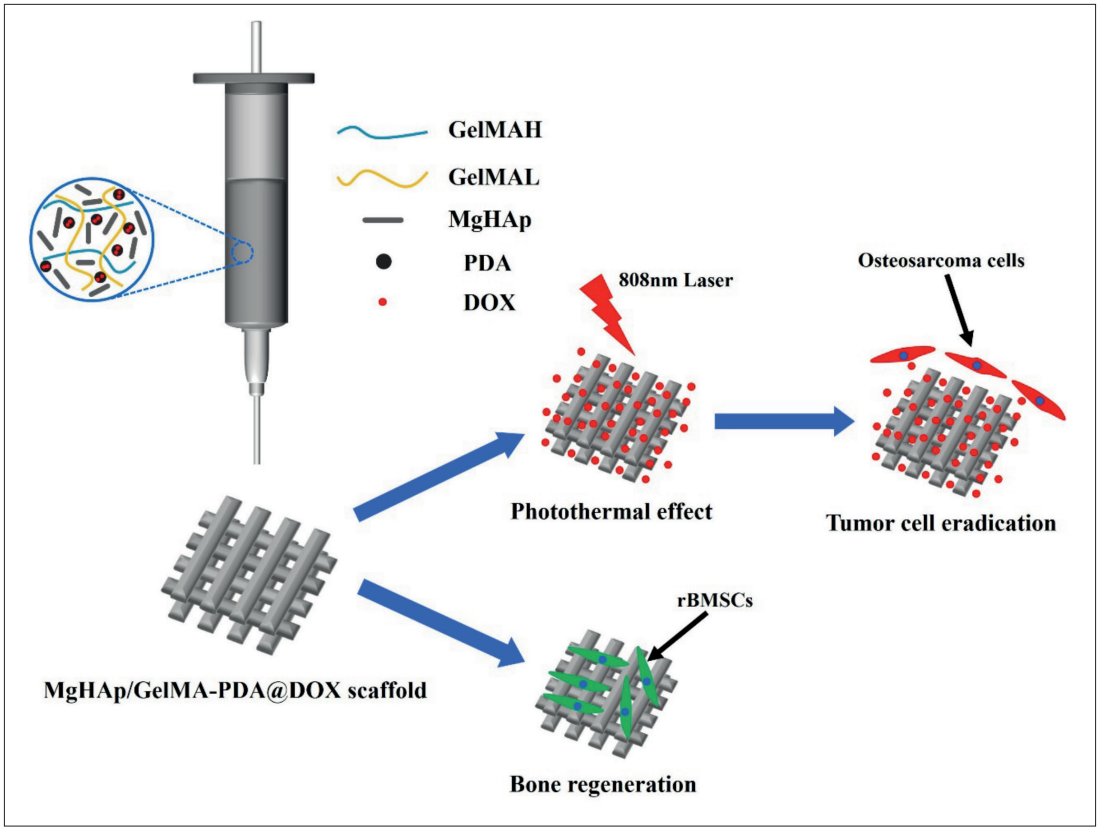

Figure 1. Schematic illustration of the fabrication of MgHAp/GelMA-PDA@DOX hydrogels using 3D printing and their dual functionality in eradicating tumor cells and promoting bone tissue regeneration.

2-methylpropiophenone, and ammonium hydroxide solution (NH_4OH; 28%) were purchased from Sigma-Aldrich (St. Louis, MO, USA). Dopamine hydrochloride (98%) and doxorubicin hydrochloride (DOX) were bought from Aladdin Co., Ltd., China. Sodium chloride (NaCl), sodium hydroxide (NaOH), anhydrous chloride ($CaCl_2$), magnesium chloride hexahydrate ($MgCl_2{\cdot}6H_2O$), disodium hydrogen phosphate dodecahydrate ($Na_2HPO_4{\cdot}12H_2O$), and ethanol were supplied by Sinopharm Chemical Reagent Co., Ltd., China. Dialysis tubing cellulose membrane (MWCO: 10 kDa) was bought from Thermo Fisher Scientific. All reagents were used as-received without further purification.

2.2. Synthesis of MgHAp nanocomposites, GelMA, and PDA@DOX particles

HAp and MgHAp nanocomposites were synthesized via a biomimetic mineralization process following the procedure as described in the previous study.[35] Briefly, 0.5 g COL1 was dissolved in 100 mL deionized (DI) water under constant magnetic at a 37°C water bath. Then, 500 mL 0.1 M $CaCl_2$, 300 mL 0.1 M Na_2HPO_4, 40 mL 1 M citric acid, and 3.6 g NaCl were added in a sequence order. Subsequently, a 4 M NaOH solution was added dropwise to adjust the pH to 9–10. The reaction system was then incubated in an incubator at 37°C for 7 days. Afterward, the white precipitate was suspended in 75% ethanol. The precipitate was centrifuged at 12,000 rpm/min for 10 min and washed with DI water three times and then freeze-dried. Finally, HAp nanocomposites were obtained and stored at 4°C for further use. For the synthesis of MgHAp nanocomposites, 500 mL 0.1 M $CaCl_2$ was replaced by 450 mL 0.1 M $CaCl_2$ and 50 mL 0.1 M $MgCl_2$, while the other procedures remained the same. The morphology and microstructure of HAp and MgHAp nanocomposites were characterized using a field emission scanning electron microscope (SEM; Hitachi S4800, Japan) and transmission electron microscope (TEM; Themis, Thermo Scientific, USA). The crystallographic phase of HAp and MgHAp nanocomposites was investigated using an X-ray diffractometer (XRD; 7000S, Shimadzu, Japan) over a range of 2θ from 10° to 70°. The characteristic groups in HAp and MgHAp nanocomposites were examined using an FT-IR spectrometer (PerkinElmer, USA) under the attenuated total reflection (ATR) mode.

Two sets of GelMA with a high degree of methacrylation (~80%) and a low degree of methacrylation (~20%) were synthesized according to the previous reported method.[26] Accordingly, GelMA with a high degree of methacrylation was designated as GelMAH, while GelMA with a low degree of methacrylation was designated as GelMAL. Briefly, 10 g gelatin was dissolved in 100 mL phosphate-buffered saline (PBS; pH 7.4, Gibco) at 50°C under constant magnetic stirring for 1 h. Subsequently, 0.8 mL (for GelMAL) or 8.0 mL (for GelMAH) methacrylic anhydride (MA) was added dropwise to the gelatin solution. The reaction continued for 3 h and was then stopped by adding five times the volume of PBS to the system. Afterward, the solution was transferred into a dialysis tubing cellulose membrane and dialyzed against DI water at 40°C for 1 week. The DI water was refreshed daily. Finally, GelMA was freeze-dried and stored at 4°C for further use. The degree of methacrylation of GelMA was characterized using ^{1}H NMR spectroscopy (Bruker Avance III 400, Germany). The secondary structure of GelMA was studied using a circular dichroism (CD) spectrometer (JASCO J-815, Japan) at 4 and 37°C, respectively. The characteristic groups of GelMA were investigated using an FT-IR spectrometer under ATR mode. Moreover, the phase transition temperatures of GelMAH and GelMAL solutions were determined using a Rheometer (MCR 302, Anton Paar, Austria).

PDA and PDA@DOX particles were synthesized following the procedure described in our previous study with slight modifications.[37] Briefly, 350 mL absolute ethanol, 12 mL NH_4OH, and 288 mL DI water were mixed homogenously under constant magnetic stirring for 30 min. Dopamine hydrochloride (2.5 g) was dissolved in 50 mL DI water. The dopamine solution was then added to the mixture for reaction at room temperature in an open-air environment for 24 h. PDA particles were obtained followed the centrifugation at 12,000 rpm/min for 10 min and subsequently dried in an oven at 80°C. PDA@DOX particles were synthesized using the same procedure but with the addition of 0.5 g DOX dissolved in the dopamine solution. The morphology and microstructure of PDA and PDA@DOX particles were examined using SEM and TEM. Moreover, the diameter of the PDA and PDA@DOX particles was calculated using the ImageJ software.

2.3. Rheological properties of printing inks

The compositions of the printing inks are listed in Table 1. Briefly, taking MgHAp/GelMA-PDA as a typical example, a 20% w/v GelMA solution was prepared by dissolving 10% w/v GelMAL and 10% w/v GelMAH in PBS at 40°C in a water bath under constant magnetic stirring. Subsequently, 2% w/v MgHAp and 0.5% w/v PDA were added to the GelMA solution. Photoinitiator was added to the printing ink with a final concentration of 0.2% w/v.

The phase transition temperatures of the printing inks were characterized from 10 to 40°C using a rotational rheometer equipped with a parallel plate unit with a 20 mm diameter and 1.0 mm measurement gap (1% strain and 1 Hz). The shear-thinning behavior of the printing inks was studied at shear rate ranging from 0.1 to 100 s^{-1} at 25°C.

Table 1. Concentrations of HAp, MgHAp, GelMA, and PDA in different printing inks.

	GelMAL (% w/v)	GelMAH (% w/v)	HAp (% w/v)	MgHAp (% w/v)	PDA (% w/v)	Photoinitiator (% w/v)
GelMA	10	10	0	0	0	0.2
HAp/GelMA	10	10	2	0	0	0.2
MgHAp/GelMA	10	10	0	2	0	0.2
MgHAp/GelMA-PDA	10	10	0	2	0.5	0.2

Abbreviations: GelMA, gelatin methacryloyl; GelMAH, GelMA with a high degree of methacrylation; GelMAL, GelMA with a low degree of methacrylation; HAp, hydroxyapatite; MgHAp, magnesium-substituted hydroxyapatite; PDA, polydopamine.

The storage moduli (G') and loss moduli (G'') of the inks subjected to a maximum strain (γ) of 1.0% were measured at a frequency range of 0.1–100 rad/s at 25°C. The G' and G'' of the inks crosslinked by UV exposure for 5 min were also measured. Moreover, the thixotropic behavior of the inks was studied by repetitive application of shear rates of 0.1 s^{-1} for 120 s and 100 s^{-1} for 60 s at 25°C.

2.4. 3D printing of MgHAp/GelMA-PDA hydrogels

3D printing of GelMA, HAp/GelMA, MgHAp/GelMA, and MgHAp/GelMA-PDA hydrogels was performed using a 3D bioprinter (3D Discovery™ Evolution, regenHU Ltd., Switzerland). The printing inks were transferred into a syringe and installed on the 3D bioprinter. The printing temperature was set to 25°C, and the printing platform was kept at room temperature. The inner diameter of printing nozzle was 0.26 mm. The printing speed was set to 8 mm/s to match the ink extrusion rate. After 3D printing, the hydrogels were exposed to 5-min UV light irradiation for covalently crosslinking GelMA polymer chains. Subsequently, the 3D-printed GelMA, HAp/GelMA, MgHAp/GelMA, and MgHAp/GelMA-PDA hydrogels were freeze-dried and stored at 4°C for further use.

2.5. Characterization of 3D-printed MgHAp/GelMA-PDA hydrogels

2.5.1. Printability of inks and structural fidelity of printed hydrogels

The printability (Pr) values of GelMA, HAp/GelMA, MgHAp/GelMA, and MgHAp/GelMA-PDA inks were calculated using the ImageJ software to measure the area and perimeter of interconnected pores of hydrogels immediately after 3D printing. Pr values were calculated using the following formula:[38]

$$Pr = \frac{L^2}{16A} \quad \text{(I)}$$

where Pr is the printability value of printing inks, L is the perimeter of the printed pore, and A is the area of the pore in the printed hydrogels.

The structural fidelity of printed GelMA, HAp/GelMA, MgHAp/GelMA, and MgHAp/GelMA-PDA hydrogels was determined using the ImageJ software by calculating the expansion percentage of printed strut. It was calculated according to the following formula:

$$Strut\ diameter\ expansion\ percentage(\%) = \frac{(D_1 - D_0)}{D_0} \times 100 \quad \text{(II)}$$

where D_1 is the diameter of printed strut of hydrogels, and D_0 is the diameter of designed strut of hydrogels.

2.5.2. Morphology and microstructure

The morphology and microstructure of printed GelMA, HAp/GelMA, MgHAp/GelMA, and MgHAp/GelMA-PDA hydrogels were determined using an SEM. Dry GelMA, HAp/GelMA, MgHAp/GelMA, and MgHAp/GelMA-PDA hydrogel samples were sputter-coated with a thin layer of gold. Then, the morphology and microstructure of the gold-coated samples were observed under SEM in a high vacuum mode at 10 kV. Additionally, to visualize the presence of MgHAp nanocomposites in hydrogel samples, the energy dispersive X-ray spectrometer (EDS) mapping was performed.

2.5.3. Mechanical properties

The mechanical properties of 3D-printed GelMA, HAp/GelMA, MgHAp/GelMA, and MgHAp/GelMA-PDA hydrogels crosslinked by UV light were determined through compression tests. Dry and wet hydrogel samples (10 mm in diameter and 5 mm in height) were compressed at a testing speed of 0.5 mm/min using a universal mechanical testing machine (Model 5848, Instron Ltd., USA), respectively. The ultimate compression strength of printed hydrogels was the highest load at the break divided by the original cross-sectional area of the hydrogel samples. Young's modulus of printed hydrogels was calculated using the slope of the initial linear section of stress–strain curves.

2.5.4. Swelling behavior and in vitro degradation

To investigate the dynamic swelling behavior, dry hydrogel samples were weighed and measured as W_0. Then, hydrogel samples were immersed in PBS at 37°C water baths. At each predetermined time point, hydrogel samples were

taken out, and the excess PBS on sample surface was gently removed. The weight of swollen hydrogel samples was measured as W_1. The swelling ratios of printed GelMA, HAp/GelMA, MgHAp/GelMA, and MgHAp/GelMA-PDA hydrogels were calculated according to the following formula:

$$Swelling\ ratio(\%) = \frac{(W_1 - W_0)}{W_0} \times 100 \quad \text{(III)}$$

where W_0 represents the weight of dry hydrogel samples, and W_1 represents the weight of swollen hydrogel samples.

To determine *in vitro* degradation behavior of 3D-printed GelMA, HAp/GelMA, MgHAp/GelMA, and MgHAp/GelMA-PDA hydrogels, the weight of each dry hydrogel sample was weighed as M_0. Afterward, hydrogel samples were immersed in 5 mL PBS supplemented with 0.02% sodium azide (NaN_3) and placed in a shaking water bath at 37°C. PBS was refreshed every 2 days. At each predetermined time point, hydrogel samples were taken out and freeze-dried. The weight of each degraded hydrogel sample was weighed as M_1. The *in vitro* degradation rate of printed hydrogels was calculated according to the following formula:

$$Degradation\ rate(\%) = \frac{(M_0 - M_1)}{M_0} \times 100 \quad \text{(IV)}$$

where M_0 represents the weight of each dry hydrogel sample, and M_1 represents the weight of each degraded hydrogel sample.

2.5.5. pH change and ion release

To study the pH changes of 3D-printed GelMA, HAp/GelMA, MgHAp/GelMA, and MgHAp/GelMA-PDA hydrogels, 0.5 g hydrogel samples were immersed in 5 mL PBS in a shaking water bath at 37°C. At each predetermined time point, pH value of the immersion liquid was detected using a pH meter. Additionally, to investigate ion release behavior of printed hydrogels, 0.5 g hydrogel samples were immersed in 5 mL PBS in a shaking water bath at 37°C. At each predetermined time point, 0.5 mL PBS was removed and another fresh 0.5 mL PBS was added. The concentration of Mg^{2+} and Ca^{2+} in PBS was determined using an inductively coupled plasma mass spectrometer (ICP-MS, ELAN DRC-e, PerkinElmer, USA).

2.6. Photothermal effect and in vitro DOX release behavior

To investigate the photothermal effect of 3D-printed GelMA, HAp/GelMA, MgHAp/GelMA, and MgHAp/GelMA-PDA hydrogels, hydrogel samples were irradiated by an NIR laser (wavelength: 808 nm) at different power densities (0.5 and 1.0 W/cm^2), respectively. At each predetermined time point, the temperatures of hydrogel samples were recorded using an infrared camera (GUIDE EasIR-9, AutoNavi, China).

To study the effect of NIR laser irradiation on DOX release, 3D-printed MgHAp/GelMA-PDA@DOX hydrogel samples were immersed in PBS and exposed to different power densities of NIR laser (0, 0.5, and 1.0 W/cm^2) for 30 min every 1 h at 37°C. At each predetermined time point, the released medium was collected, and an equal amount of PBS was replenished. The amount of DOX in the released medium was measured using a UV–vis spectrometer (UV-2600, Shimadzu, Japan) at the wavelength of 480 nm. The cumulative release curves of DOX were then established. Furthermore, to determine the pH-responsive DOX release behavior of MgHAp/GelMA-PDA@DOX hydrogels, hydrogel samples were immersed in pH 4.5 and pH 7.4 buffer solutions at 37°C, respectively. At each predetermined time point, the release medium was collected, and an equal amount of fresh buffer solution was added. The amount of DOX released was measured using a UV–vis spectrometer at the wavelength of 480 nm. The cumulative release curves of DOX were then established.

2.7. *In vitro* antitumor efficiency

In the current study, MG63 osteosarcoma cells were used to evaluate the antitumor efficiency of 3D-printed MgHAp/GelMA-PDA@DOX hydrogels. MG63 cells at a density of 1×10^4 cells per well were seeded on the hydrogel samples in a 24-well cell culture plate. Hydrogel samples were cultured in the Dulbecco's modified eagle medium (DMEM; Gibco) supplemented with 10% v/v fetal bovine serum (FBS; Gibco) and 1% v/v penicillin/streptomycin (Gibco) in a CO_2 incubator at 37°C. Hydrogel samples were irradiated with an 808 nm NIR laser for 5 min every day. After culturing for 4 and 24 h, a live/dead assay (Invitrogen, Thermo Fisher Scientific) was employed to determine the survival rate of MG63 cells cultured on the hydrogel samples. Moreover, the cell viability of MG63 cells on the hydrogel samples was assessed using 3-(4,5-dimethylthiazol-2-yl)-2,5 diphenyl tetrazolium bromide (MTT; Invitrogen, Thermo Fisher Scientific) tests at each predetermined time point (1, 3, and 5 days).

2.8. Proliferation and osteogenic differentiation of rBMSCs on 3D-printed scaffolds

The proliferation behavior of rBMSCs on 3D-printed MgHAp/GelMA-PDA hydrogels was studied through MTT tests. Briefly, rBMSCs at a density of 1×10^4 cells per well were seeded on hydrogel samples in a 24-well cell culture plate and cultured in medium in a CO_2 incubator at

37°C. After culturing for 1, 3, and 7 days, cell proliferation was evaluated using the MTT assay.

To investigate the effect of Mg^{2+} release on rBMSCs osteogenic differentiation, 1×10^5 cells per well were seeded on hydrogel samples in a 24-well cell culture plate. Following a culture period of 3 days, the culture medium was replaced by an osteogenic differentiation medium (which was prepared by adding 0.1 mM dexamethasone, 50 mM ascorbic acid, and 10 mM β-sodium glycerophosphate in culture medium). After culturing for 7 and 14 days, the activity of alkaline phosphatase (ALP) of rBMSCs on the hydrogel samples was measured using an ALP assay (Wako, Japan) according to the manufacturer's protocol. Additionally, the total protein concentration was measured using the BCA kit (Thermo Fisher Scientific). Moreover, the expression of ALP was assessed by means of ALP staining. Briefly, after being cultured in osteogenic differentiation medium for 14 days, rBMSCs were fixed with 4% paraformaldehyde (Sigma-Aldrich, St Louis, MO, USA) for 15 min, washed with PBS, and incubated with ALP staining solution for 30 min in the dark. The images were recorded using a microscope (Leica DMi8, Germany).

Furthermore, the expression of osteogenesis-related genes, such as osteocalcin (*Ocn*), *Col1*, runt-related transcription factor-2 (*Runx2*), and bone morphogenetic protein-2 (*Bmp2*) was studied using quantitative real-time polymerase chain reaction (qRT-PCR) analysis. Briefly, after culturing rBMSCs on hydrogel samples in osteogenic medium for 14 days, the total RNA was extracted using Trizol reagent (Servicebio, China). The obtained RNA was reverse-transcribed to complementary DNA (cDNA) using the Revert-Aid First Strand cDNA Synthesis Kit (Thermo Fisher Scientific). Then, qRT-PCR analysis was performed. Housekeeping gene glyceraldehyde 3-phosphate dehydrogenase (*Gapdh*) was used as the control to normalize the expression of osteogenesis-related genes. The $2^{-\Delta\Delta Ct}$ method was used to calculate the mRNA expression levels. The sequences of the primers ae listed in Table S1, Supporting Information.

In addition, after being cultured in osteogenic medium for 14 days, rBMSCs on hydrogel samples were fixed with 4% paraformaldehyde for 15 min and then incubated with anti-COLI rabbit primary antibody (Abcam) for 1 h and then FITC-conjugated goat anti-rabbit secondary antibody (Santa Cruz Biotechnology Inc., USA) for 1 h. Cell nuclei were stained with DAPI solution. The morphology of rBMSCs was examined using a confocal laser scanning microscope (Leica DMi8, Germany).

2.9. Statistical analysis

The results presented in the current study were obtained from at least three separate samples or tests and are expressed as the mean ± standard deviation (SD). One-way analysis of variance (ANOVA) was performed to carry out statistical analysis. Data analyses in the current study were conducted using Excel and SPSS.

Differences were considered statistically significant when $p < 0.05$, $p < 0.01$, and $p < 0.001$.

3. Results and discussion

3.1. Synthesis and characterization of MgHAp, GelMA, and PDA@DOX

Previous studies have employed biomimetic self-assembly mineralization method to fabricate HAp to mimic the structure and composition of natural bone.[39] As a result, HAp synthesized through biomineralization process exhibited a positive effect on cell activities (e.g., cell attachment, proliferation, and differentiation) and could promote new bone formation. Moreover, considering the inherent components of natural bone, i.e., inorganic HAp, organic COL1 and citric acid, research employing COL1 and citric acid as bitemplate for HAp nanocomposites synthesis emerged as COL1 enabled to modulate nucleation sites and crystal growth of HAp due to its well-organized fiber orientation, while citric acid could regulate HAp formation owing to its abundant carboxyl groups.[35,40] Therefore, in the current study, HAp nanocomposites with a great similarity in structure and composition of apatite in natural bone were synthesized using COL1 and citric acid as bitemplate through a biomineralization process. Magnesium is an important metal element in human body, with 60% present in the human bone. Studies have indicated that Mg^{2+} played an essential role in bone metabolism by regulating osteoblast and osteoclast activities.[36,41] Moreover, compared to HAp, MgHAp could promote cell proliferation and osteogenic differentiation through activating integrin on the cell surface.[42] Thus, MgHAp was synthesized in the current work for investigation. As shown in Figure 2A, the morphology of both HAp and MgHAp nanocomposites exhibited a plate-like structure, and the size of HAp and MgHAp nanocomposites was around 40–70 nm, showing great similarity to the shape of apatite in natural bone. Figure 2B and C show the element compositions of HAp and MgHAp nanocomposites. Notably, there was a small amount of Mg element in the EDS spectrum, as shown in Figure 2C, indicating the presence of Mg^{2+} in MgHAp nanocomposites. As shown in Figure 2D, XRD patterns showed that HAp and MgHAp nanocomposites were mainly hydroxyapatite phase. However, due to the incorporation of COL1 and citric acid in the nanocomposites, HAp and MgHAp showed a low crystallinity in comparison to pure hydroxyapatite mineral. Furthermore, compared to HAp nanocomposites, MgHAp nanocomposites exhibited an even lower crystallinity due

to the substitution of Mg^{2+} in hydroxyapatite phase. The FT-IR spectra in Figure 2E confirmed the compositions of HAp and MgHAp nanocomposites. The characteristic peaks at 1032.8 and 1037.6 cm^{-1} were attributed to the antisymmetric P–O stretching, while the peaks at 563.1 and 565.1 cm^{-1} were due to O–P–O bending of hydroxyapatite. Additionally, the characteristic peaks at 3444.4 and 3438.6 cm^{-1} might be attributed to the vibrations of O–H of water and N–H of COL1. The amide I band in COL1 and carboxyl groups in citric acid appeared at 1596.8 and 1608.44 cm^{-1} respectively.

GelMA is a popular biomaterial for 3D printing due to its remarkable temperature-responsive behavior, forming triple-helix structure in the gel state at low temperatures while exhibiting random coil structure in the sol state upon heating.[26] Additionally, GelMA exhibits good photocurable properties and can be covalently crosslinked upon visible or UV light irradiation to form stable hydrogel networks.[43] Previous studies have indicated that the temperature-responsive behavior and photocurable properties of GelMA were significantly affected by the degree of methacrylation.[44,45] GelMA with a high degree of methacrylation has a low sol–gel transition temperature, which is not beneficial for extrusion-based 3D printing. When crosslinked by UV light, GelMA with a high degree of methacrylation can exhibit high mechanical strength, making it more suitable for bone tissue engineering. On the contrary, GelMA with a low degree of methacrylation has a high sol–gel transition temperature, which makes it more suitable for extrusion-based 3D printing. However, GelMA with a low degree of methacrylation can have low mechanical strength. A high sol–gel transition temperature can provide convenience for 3D printing, while a high mechanical strength is beneficial for bone tissue regeneration. Therefore, in the current study, GelMAH (high degree of methacrylation) and GelMAL (low degree of methacrylation) were synthesized in PBS. As shown in Figure 3A, the ^1H NMR spectra showed that new peaks around 6.00–5.86 ppm (m, -O-CH_2-CH=CH_2) and 5.38–5.22 ppm (t, -O-CH_2-CH=CH_2) appeared in GelMAH and GelMAL polymer chains. Additionally, the increased intensity of the methyl peak at ~1.8 ppm and the reduced intensity of the lysine methylene peak at 2.8–3.0 ppm further showed the successful substitution of methacrylate groups in GelMAH and GelMAL. Degrees of methacrylation of GelMAH and GelMAL calculated using the 2,4,6-trinitrobenzenesulfonic acid (TNBS) method were ~80% and ~20%, respectively (Figure 3B). The CD spectra presented in Figure 3C suggested that the methacryloylation of GelMA had an impact on the secondary structure. The intensity at 198 nm is ascribed to the random coil structure formation, and the intensity at 222 nm results from the formation of triple helix structure. As shown in Figure 3C, Gel exhibited a higher intensity at 222 nm at 4°C than GelMAH and GelMAL, suggesting that the formation of methacrylate groups in GelMA chains influences the interactions between GelMA polymer chains and therefore slightly interfered with the secondary structure. The FT-IR spectra in Figure 3D indicated that GelMAH and GelMAL preserved the characteristic peaks (amide I, amide II, amide III) of gelatin. Furthermore, Figure 3E indicates that the sol–gel temperatures of Gel, GelMAH, and GelMAL are 32.9, 27.7, and 30.8°C, respectively. GelMAH had a high degree of methacrylation and therefore imparted a high interference to the secondary structure, thereby resulting in a low sol–gel temperature.

Due to the excellent adhesive property, biocompatibility and good photothermal effect, PDA particles have been widely used as drug carriers and can provide controlled and sustained *in situ* drug delivery.[46] In the current study, DOX was encapsulated in PDA particles to fabricate PDA@DOX particles via *in situ* polymerization in a weakly alkaline solution.[37] As shown in Figures 4 and S1, Supporting Information, the PDA and PDA@DOX particles were spherical in shape, with an average diameter of 227.5 ± 3.1 and 161.8 ± 9.1 nm, respectively. The encapsulation of DOX in PDA particles did not significantly affect the morphology and diameter of the PDA@DOX particles.

3.2. Rheological properties of printing inks

As mentioned, GelMA with a low degree of methacrylation exhibits a high sol–gel transition temperature and thus is beneficial for 3D printing. However, GelMA with a low degree of methacrylation usually possesses low mechanical strength, which is not suitable for bone tissue regeneration.[47] On the contrary, GelMA with a high degree of methacrylation usually has a low transition temperature and possesses high mechanical strength when crosslinked by UV light. In the current study, to develop an optimal printing ink for 3D printing and bone tissue regeneration, GelMA inks consisting of 10% GelMAH and 10% GelMAL were prepared. As shown in Figures 5A and S2, Supporting Information, the sol–gel transition temperatures of GelMA, HAp/GelMA, MgHAp/GelMA, and MgHAp/GelMA-PDA inks were 31.5, 33.6, 29.4, and 31.8°C, respectively. The gel–sol transition temperatures of GelMA, HAp/GelMA, MgHAp/GelMA, and MgHAp/GelMA-PDA inks were 30.8, 30.9, 29.8, 35.7°C, respectively (Figure 5B). All printing inks exhibited high transition temperatures above 29°C, providing great convenience for extrusion-based 3D printing.

For extrusion-based 3D printing, the viscosity of inks is essential for achieving good extrudability.[48] If the viscosity is too low, inks can easily leak from the nozzle

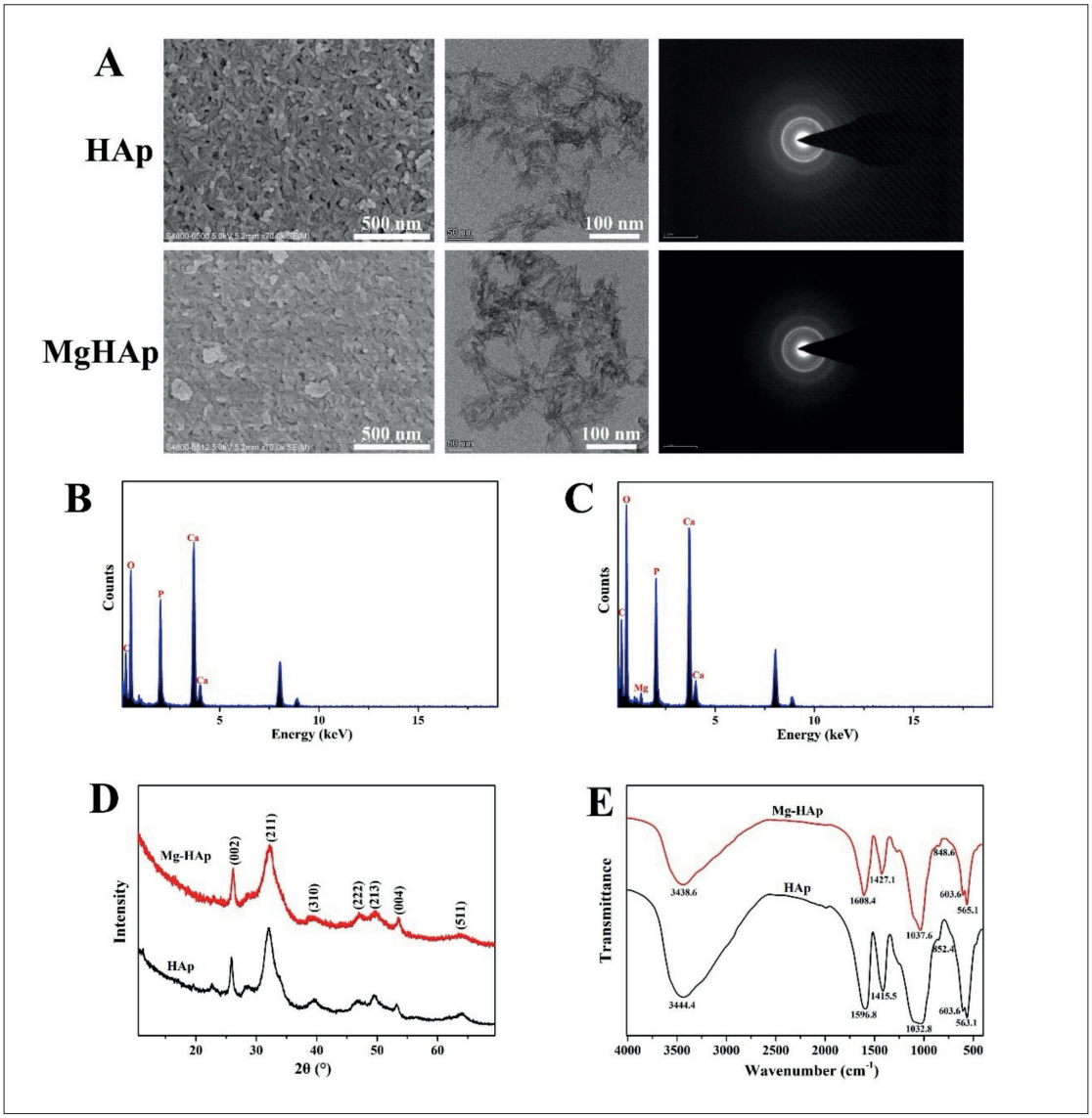

Figure 2. Characterization of HAp and MgHAp nanocomposites. (A) SEM and TEM images showing the morphology and structure of HAp and MgHAp nanocomposites. (B, C) EDS spectra of HAp (B) and MgHAp (C) nanocomposites. (D, E) XRD patterns (D) and FT-IR spectra (E) of HAp and MgHAp nanocomposites.

of the printing head, resulting in difficulty in maintaining the structural stability of printed hydrogels. On the other hand, if the viscosity is too high, the inks are semi-solid and hence high pressures are required for extrusion; otherwise, the inks may not be extruded from the nozzle. Therefore, a good or desirable printing ink should exhibit a shear-thinning behavior, like non-Newtonian fluids, characterized by decreasing viscosity with an increase in shear rate.[49] As shown in Figure 5C, GelMA, HAp/GelMA, MgHAp/GelMA, and MgHAp/GelMA-PDA inks exhibited excellent shear-thinning behavior over an increase in shear rate from 0.1 to 1000 s^{-1}, indicating that all inks were suitable for 3D printing. The rheological properties of GelMA, HAp/GelMA, MgHAp/GelMA, and MgHAp/GelMA-PDA inks, with or without UV crosslinking, were determined through frequency sweep tests. Figure 5D indicates that the G' values of all inks without UV crosslinking were higher than G'' at 25 °C, suggesting the elastic state of inks. It might be attributed to the 20% GelMA in the inks. Additionally, UV crosslinking led to the dramatic increase of G' and G'' values of all inks (Figure 5E), as a result of the crosslinking of GelMA chains, which contributed to the formation of robust hydrogel networks. Furthermore, the thixotropic behavior of the inks was investigated under the repeated application of a low shear rate (0.1 s^{-1}) for 120 s and a high shear rate (100 s^{-1}) for 60

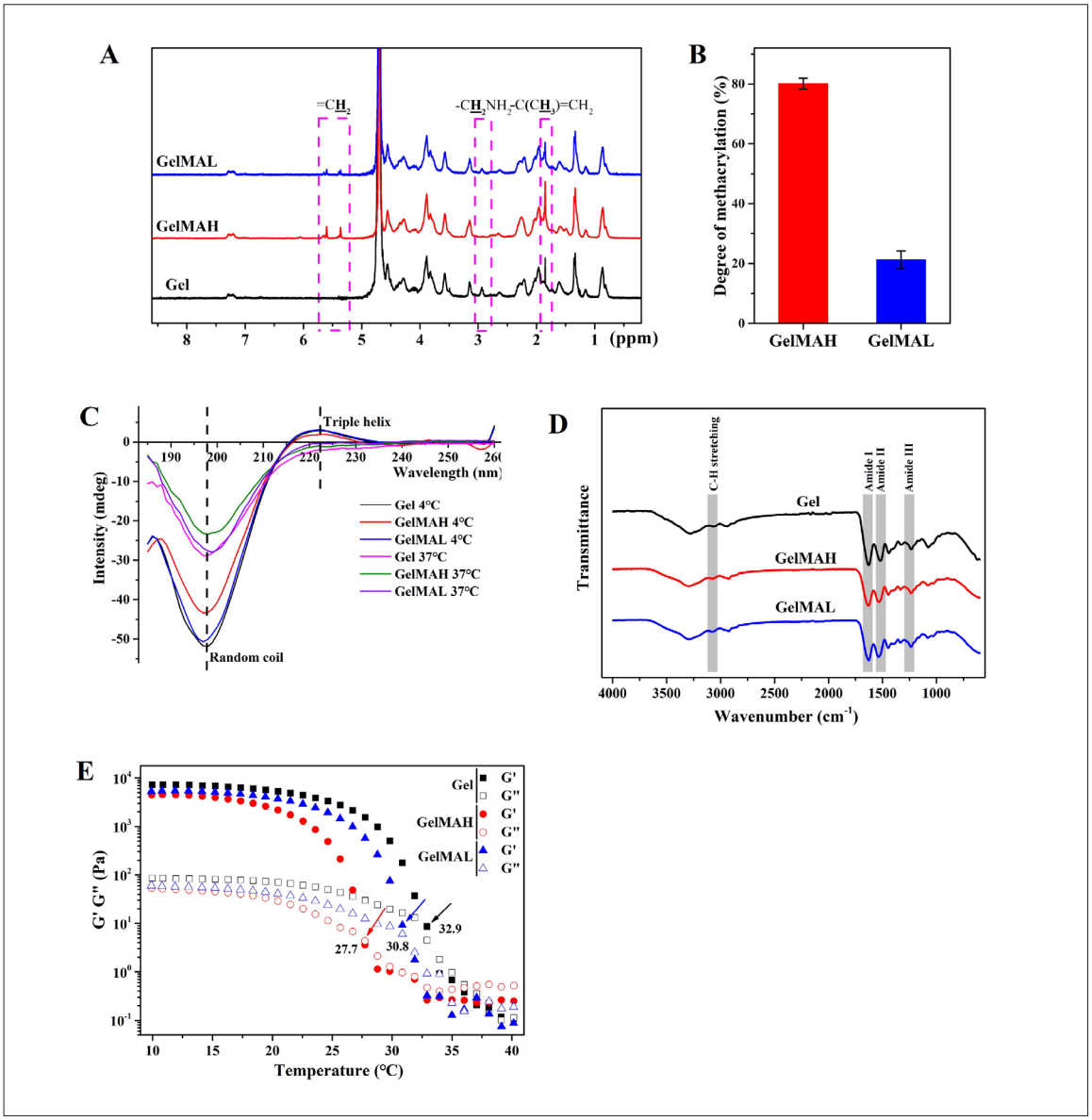

Figure 3. Characterization of GelMAH and GelMAL. (A) ^{1}H NMR spectra of Gel, GelMAH, and GelMAL. (B) Degree of methacrylation of GelMAH and GelMAL calculated using the 2,4,6-trinitrobenzenesulfonic acid (TNBS) method. (C) Circular dichroism (CD) spectra of Gel, GelMAH, and GelMAL at 4 and 37°C, respectively. (D) FT-IR spectra of Gel, GelMAH, and GelMAL. (E) Variation of *G′* and *G″* in terms of temperature for Gel, GelMAH, and GelMAL. Abbreviations: Gel, gelatin; GelMAH, GelMA with a high degree of methacrylation; GelMAL, GelMA with a low degree of methacrylation.

s. As shown in Figure 5F, GelMA, HAp/GelMA, MgHAp/GelMA, and MgHAp/GelMA-PDA inks all possessed excellent thixotropic behavior. The viscosity of the inks dramatically decreased when subjected to a high shear rate and immediately recovered to the original state after the removal of shear rate. These results confirmed that GelMA, HAp/GelMA, MgHAp/GelMA, and MgHAp/GelMA-PDA inks could be easily extruded from the printing nozzle and would be suitable for extrusion-based 3D printing.

3.3. Properties and characterization of 3D printed scaffolds

The printability of inks plays a crucial role in assessing their suitability for 3D printing.[50,51] Printability refers to the ability of a printing ink to be continuously and consistently printed, while forming stable 3D structures in accordance with the design during and after printing process. Printability has an impact on the physical properties (e.g., pore shape, pore size, and porosity) of printed structures, thereby determining their mechanical properties and

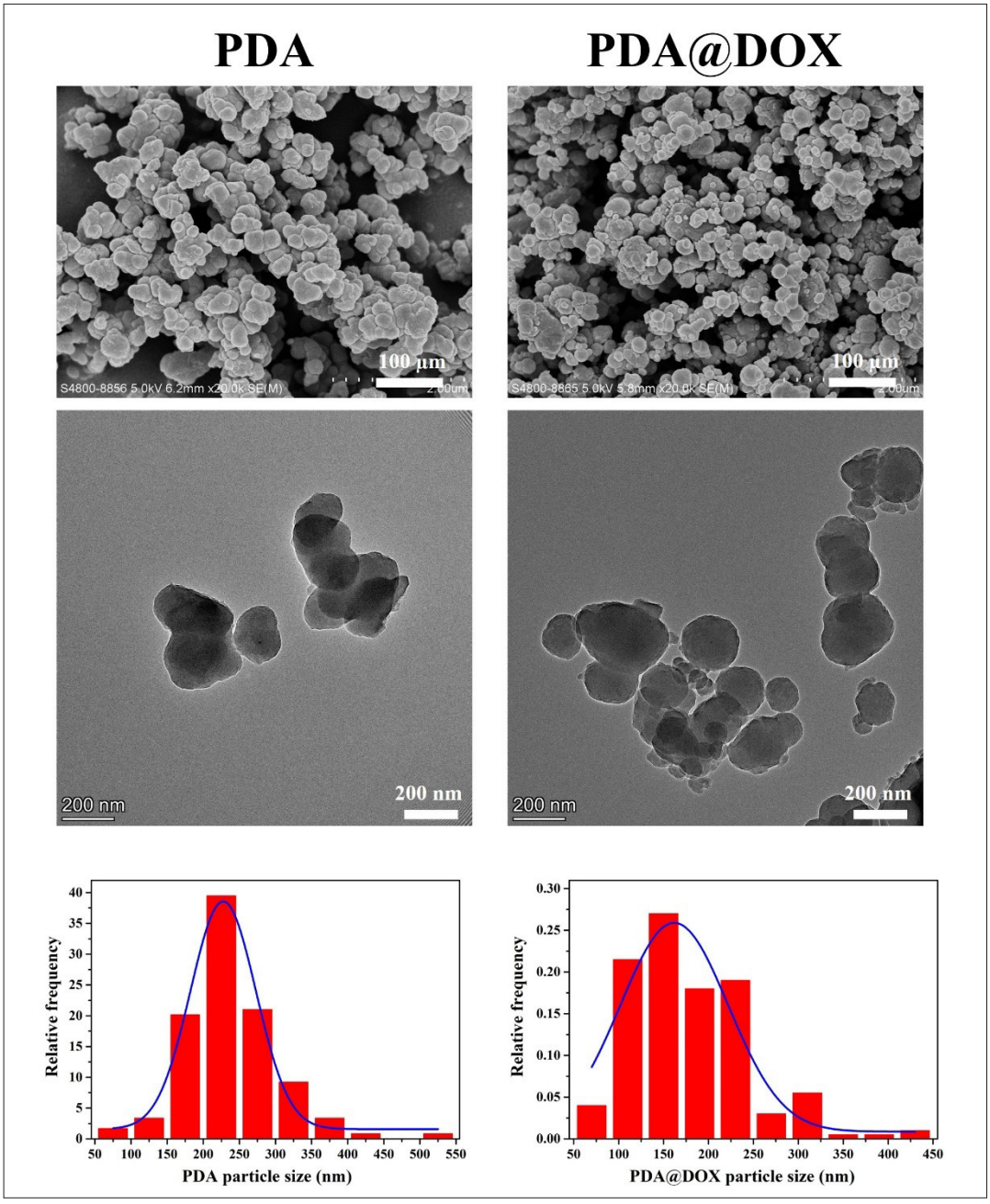

Figure 4. SEM and TEM images showing the morphology and particle size of PDA and PDA@DOX particles, and the size distribution of PDA and PDA@DOX particles.

biological performance. In the current study, a 20% GelMA inks composed of 10% GelMAH and 10% GelMAL were used to improve the printability. As calculated from the optical images showing the morphology of printed hydrogels (Figure 6A), the printability value of GelMA inks was approximately 0.875 ± 0.007, which was much better than those described in previous studies (Figure 6B).[24,52] The printability values of 3D-printed HAp/GelMA, MgHAp/GelMA, and MgHAp/GelMA-PDA inks were 0.962 ± 0.087, 1.090 ± 0.128, and 0.905 ± 0.015, respectively. The addition of HAp and MgHAp nanocomposites improved the printability. On the other hand, fidelity is an important factor in determining the ability to maintain the structure of printed objects.[53,54] It is an index that is commonly used to evaluate the similarity between the structure of printed objects and their design. Printed

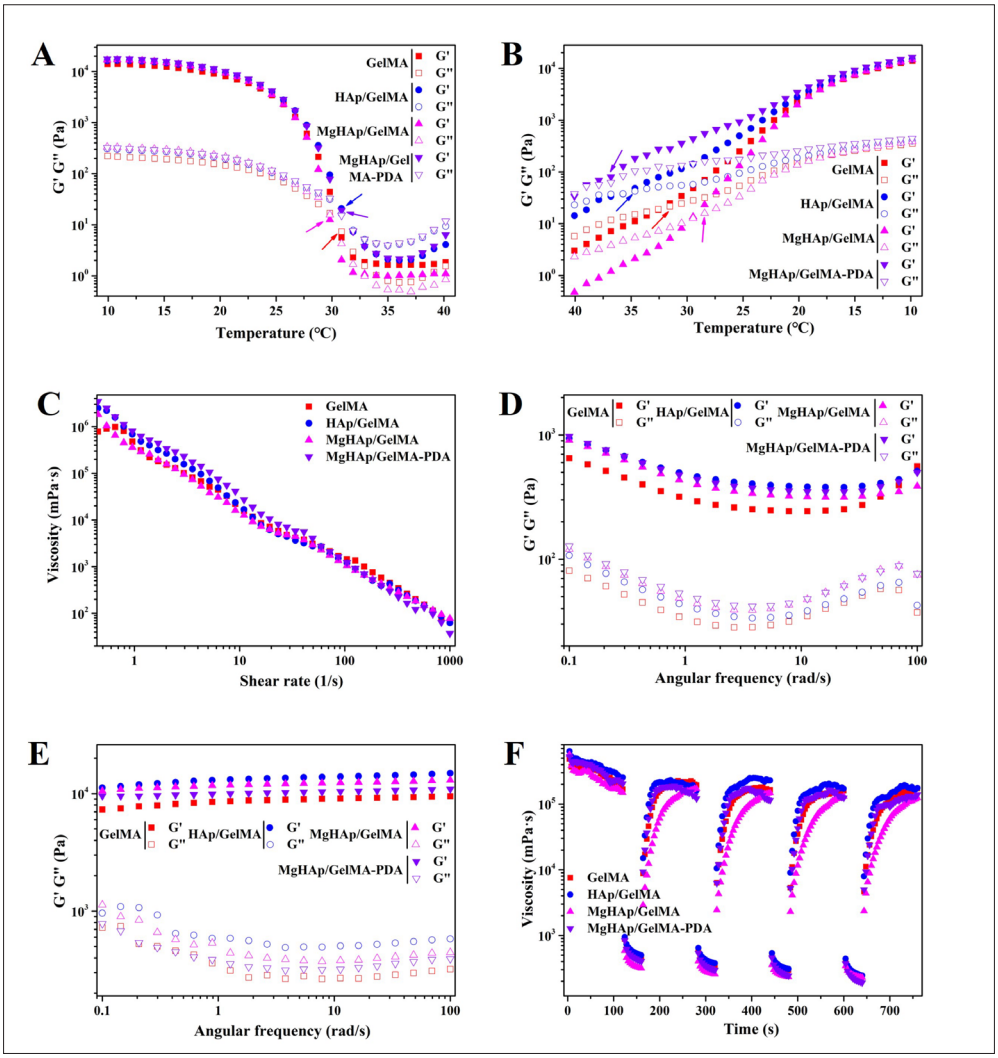

Figure 5. Rheological properties of the printing inks. (A, B) Inks from gel state to sol state (A), and inks from sol state to gel state (B). (C) Shear thinning behavior of GelMA, HAp/GelMA, MgHAp/GelMA, and MgHAp/GelMA-PDA inks. (D) Variation of *G′* and *G″* in terms of angular frequency of GelMA, HAp/GelMA, MgHAp/GelMA, and MgHAp/GelMA-PDA inks. (E) Variation of *G′* and *G″* in terms of angular frequency of GelMA, HAp/GelMA, MgHAp/GelMA, and MgHAp/GelMA-PDA inks crosslinked by UV light. (F) Thixotropic behavior of GelMA, HAp/GelMA, MgHAp/GelMA, and MgHAp/GelMA-PDA inks.

structures with poor fidelity can lead to the deformation of printed struts, which increases the width and decreases the thickness of struts. In the current study, the struct diameter expansion rate was employed to assess the fidelity of printed hydrogels. As shown in Figure 6C, the struct diameter expansion rates of 3D-printed GelMA, HAp/GelMA, MgHAp/GelMA, and MgHAp/GelMA-PDA hydrogels were 38.51 ± 7.56%, 53.60 ± 5.73%, 39.52 ± 5.37%, and 93.54 ± 11.33%, respectively. GelMA, HAp/GelMA, and MgHAp/GelMA hydrogels exhibited similar fidelity, whereas the addition of PDA particles caused the decrease in fidelity in the MgHAp/GelMA-PDA hydrogel, which might be attributed to PDA particles interfering with the interactions between GelMA chains.

Figure 6D shows the surface and cross-sectional morphology and microstructure of dried 3D-printed GelMA, HAp/GelMA, MgHAp/GelMA, and MgHAp/GelMA-PDA hydrogels crosslinked by UV light. Hydrogels all exhibited interconnected macro-pores, which facilitated oxygen and nutrients transportation and the removal of waste, thereby promoting vascularization and tissue regeneration.[55] Moreover, 3D-printed GelMA, HAp/GelMA, MgHAp/GelMA, and MgHAp/GelMA-PDA hydrogels possessed micro-pores, which were beneficial for cell infiltration, ingrowth, and micro-blood vessels

formation.[56] The EDS mapping images shown in Figure 6D indicate the element distribution in the cross-sectional area of the printed MgHAp/GelMA hydrogel. It clearly showed the distribution of MgHAp nanocomposites in MgHAp/GelMA hydrogel. Also, EDS pattern in Figure S3, Supporting Information reveals the presence of Mg in the printed MgHAp/GelMA-PDA hydrogel. Furthermore, the thermogravimetric analysis (TGA) results in Figure S4, Supporting Information shows the thermal degradation behavior of 3D-printed GelMA, HAp/GelMA, MgHAp/GelMA, and MgHAp/GelMA-PDA hydrogels. This indicates that due to the addition of HAp and MgHAp nanocomposites, the remained weight percentages of HAp/GelMA, MgHAp/GelMA, and MgHAp/GelMA-PDA scaffolds increased after sintering at 800°C in comparison to that of GelMA hydrogel. However, the fastest thermal degradation temperature stayed nearly the same for GelMA (333.6°C), HAp/GelMA (324.1°C), MgHAp/GelMA (333.5°C), and MgHAp/GelMA-PDA (337.8°C) hydrogels. Overall, HAp and MgHAp nanocomposites were well-dispersed in the printed hydrogels.

Generally, GelMA hydrogels have poor mechanical properties. For example, Rizwan et al. found that the compression modulus of 15% GelMA hydrogels was below 50 kPa.[57] O'connell et al. showed that the peak storage modulus of 10% GelMA hydrogels could not exceed 10 kPa, even with a high photoinitiator concentration and light intensity and a long exposure time of UV light.[58] Consequently, ceramic particles were encapsulated in GelMA hydrogels to reinforce their mechanical strength.[25] In the current study, the mechanical properties of 3D-printed GelMA, HAp/GelMA, MgHAp/GelMA, and MgHAp/GelMA-PDA hydrogels were investigated through compression tests. As shown in Figures 7 and S5, Supporting Information the compression strength of 3D-printed GelMA hydrogels in the wet and dry states was 0.124 ± 0.014 and 2.590 ± 0.475 MPa, respectively. The combination of GelMAH and GelMAL significantly increased the mechanical strength because GelMAH could be efficiently crosslinked by UV light and GelMAL had a high sol–gel transition temperature and thus could be efficiently thermally crosslinked. On the other hand, the addition of 10% HAp or MgHAp in GelMA hydrogels significantly increased mechanical strength. The compression strength of 3D-printed HAp/GelMA and MgHAp/GelMA hydrogels in the wet state was 0.171 ± 0.011 and 0.182 ± 0.023 MPa, respectively. However, the compression strength of MgHAp/GelMA-PDA hydrogels in the wet state decreased to 0.099 ± 0.012 MPa, which could be attributed to the addition of PDA particles decreasing the UV crosslinking efficiency. As a result, the Young's modulus of GelMA, HAp/GelMA, MgHAp/GelMA, and MgHAp/GelMA-PDA hydrogels in the wet state were 0.114 ± 0.005, 0.195 ± 0.033, 0.211 ± 0.019, and 0.111 ± 0.059 MPa, respectively. While in the dry state, the Young's modulus of GelMA, HAp/GelMA, MgHAp/GelMA, and MgHAp/GelMA-PDA hydrogels were 10.020 ± 3.343, 28.750 ± 9.248, 36.190 ± 11.186, and 31.913 ± 10.770 MPa, respectively. Notably, the mechanical strength of 3D-printed MgHAp/GelMA-PDA hydrogels was still far behind that of the native bone. Hydrogel scaffolds usually possess insufficient mechanical strength for bone tissue regeneration. To reinforce the mechanical properties of hydrogels, ceramic particles have been widely used. In the current study, the addition of 10% of MgHAp significantly increased the modulus of hydrogels in both dry and wet state. To further improve the mechanical properties, more MgHAp nanocomposites could be incorporated into hydrogels. However, a higher percentage of MgHAp can lead to the formation of a compact network within hydrogels, thereby impacting the swelling and degradation behavior of MgHAp/GelMA-PDA hydrogels as well as influencing DOX release and cellular metabolism. Hence, striking a balance among the mechanical properties of hydrogels is critical.

The swelling behavior of hydrogels is related to their structural and dimensional stability as hydrogels tend to swell upon interaction with biological fluids, leading to changes in weight and size. Therefore, the swelling behavior of hydrogels is essential for diffusion/migration of encapsulated small biomolecules, drugs, and cells.[59] As shown in Figure 8A, printed hydrogels reached their swelling equilibrium after being immersed in PBS for 12 h. The swelling ratios of GelMA, HAp/GelMA, MgHAp/GelMA, and MgHAp/GelMA-PDA hydrogels were 328.05 ± 9.01%, 326.64 ± 3.97%, 322.01 ± 3.77%, and 307.59 ± 7.41%, respectively. The degradation of a hydrogel could facilitate the formation of extracellular matrix (ECM), thereby creating an optimal microenvironment for cell growth.[60] Moreover, the biodegradation rate of hydrogels should be compatible with the rate at which new tissue is formed. Figure 8B displays the *in vitro* degradation behavior of the printed hydrogels. Printed GelMA, HAp/GelMA, and MgHAp/GelMA hydrogels manifested similar degradation behavior. Following an immersion in PBS for 4 weeks, the degradation rates of GelMA, HAp/GelMA, and MgHAp/GelMA hydrogels were 50.41 ± 1.27%, 54.40 ± 0.85%, and 60.87 ± 0.99%, respectively. However, MgHAp/GelMA-PDA hydrogels exhibited a higher degradation rate. After 4 weeks of degradation, the degradation rate of MgHAp/GelMA-PDA hydrogels was 84.32 ± 0.79%. The relatively high degradation rate was attributed to the addition of PDA particles, which reduced the UV crosslinking efficiency.

Figure 8C–E graphically represents the changes of pH value, Ca^{2+}, and Mg^{2+} in PBS after soaking GelMA, HAp/GelMA, MgHAp/GelMA, and MgHAp/GelMA-PDA hydrogels in PBS for 2 weeks. As shown in Figure 8C, the change of pH of hydrogels appeared to be similar. The pH of GelMA, HAp/GelMA, MgHAp/GelMA, and MgHAp/GelMA-PDA hydrogels reduced on the first day, followed by an increase in the next 13 days. The Ca^{2+} release profiles in Figure 8D indicated that printed HAp/GelMA, MgHAp/GelMA, and MgHAp/

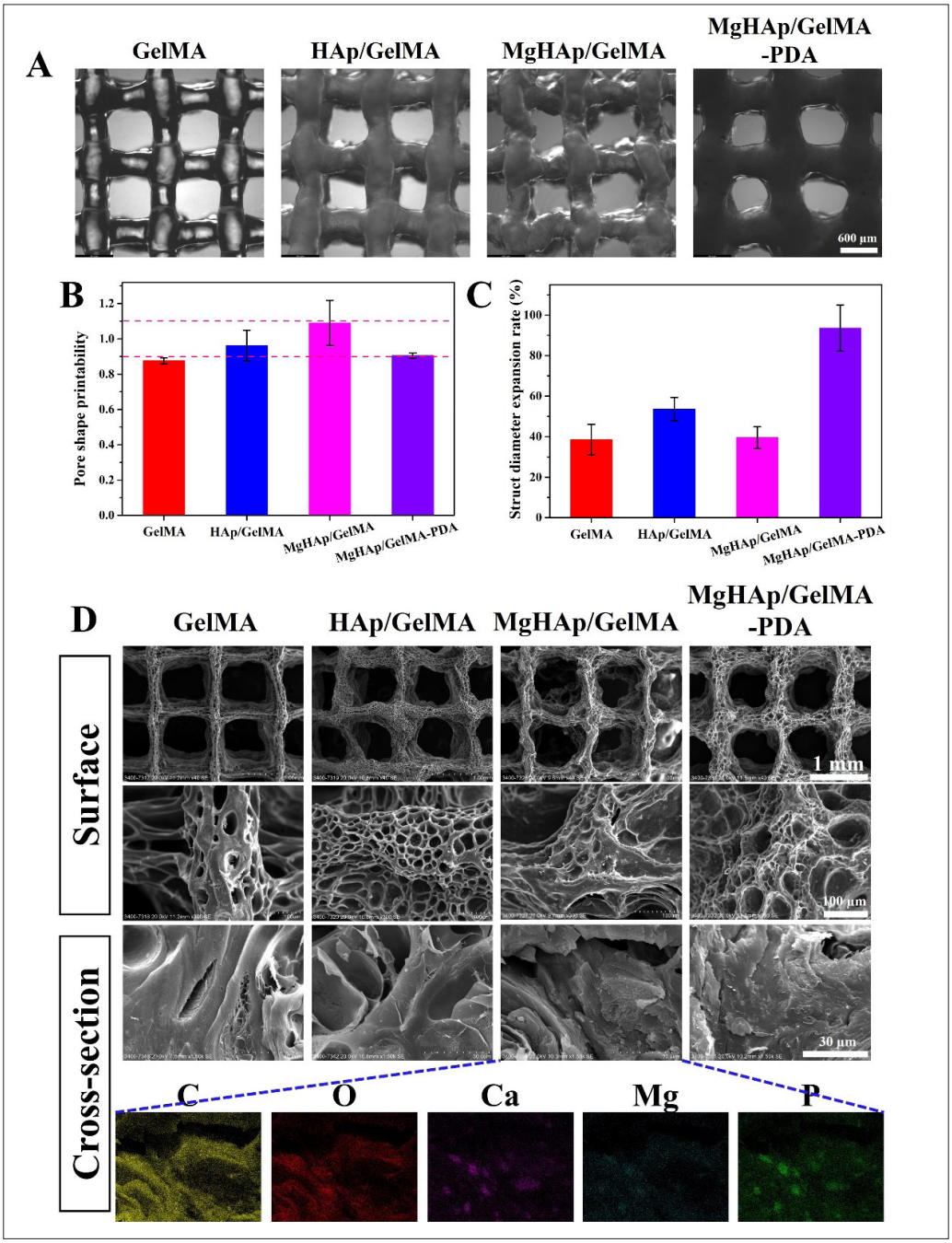

Figure 6. Morphology and structure of 3D-printed hydrogels. (A) Optical images showing the morphology and structure of GelMA, HAp/GelMA, MgHAp/GelMA, and MgHAp/GelMA-PDA hydrogels after 3D printing. (B) Printability values of GelMA, HAp/GelMA, MgHAp/GelMA, and MgHAp/GelMA-PDA inks. (C) Struct diameter expansion rates of GelMA, HAp/GelMA, MgHAp/GelMA, and MgHAp/GelMA-PDA hydrogels. (D) Surface and cross-sectional morphology of 3D-printed GelMA, HAp/GelMA, MgHAp/GelMA, and MgHAp/GelMA-PDA hydrogels and EDS mapping images showing the element distribution in the MgHAp/GelMA hydrogel.

GelMA-PDA hydrogels exhibited almost the same release trend. Furthermore, the MgHAp/GelMA and MgHAp/GelMA-PDA hydrogels shared the similar Mg^{2+} release profile. The concentrations of Ca^{2+} and Mg^{2+} gradually increased with the immersion time, suggesting the sustained release of Ca^{2+} and Mg^{2+} from MgHAp/GelMA and MgHAp/GelMA-PDA hydrogels.

3.4. Photothermal effect and *in vitro* release of DOX

As aforementioned, constructing an on-site controlled anti-tumor drug delivery system assisted by PTT enables to greatly advance tumor treatment due to the synergy of chemotherapy and induced hyperthermia.[5,61] PDA particles are highly biocompatible and have been widely used as photothermal agent for controlled drug release due to their relatively high photothermal conversion efficiency. In addition, the abundant catechol and amine groups on PDA nanoparticles confer substantial adhesive capabilities that enable high drug loading efficiency.[62] Therefore, in the current study, anti-tumor drug, DOX, was loaded in PDA particles to form PDA@DOX particles. Moreover, PDA@DOX particles were loaded in 3D-printed hydrogels for providing combined therapy and synergistic effect. Firstly, the photothermal behavior of 3D-printed GelMA, HAp/GelMA, MgHAp/GelMA, and MgHAp/GelMA-PDA hydrogels was investigated. Figure 9A–C shows the temperature changes of hydrogels when they were irradiated by an 808 nm NIR laser at different power densities (0.5 and 1.0 W/cm^2). After being irradiated by NIR laser at 0.5 and 1.0 W/cm^2 for 3 min, MgHAp/GelMA-PDA hydrogels were heated to 42.7 and 48.4°C, respectively. Previous studies have indicated that tumor cells were efficiently killed when the local temperature had gone up to 42–50°C.[63] In this context, MgHAp/GelMA-PDA@DOX hydrogels could provide effective hyperthermic ablation of tumor cells when implanted at the tumor resection site of the body. Furthermore, to determine the effect of NIR laser irradiation on DOX release, 3D-printed MgHAp/GelMA-PDA@DOX hydrogels were used. As a result, more

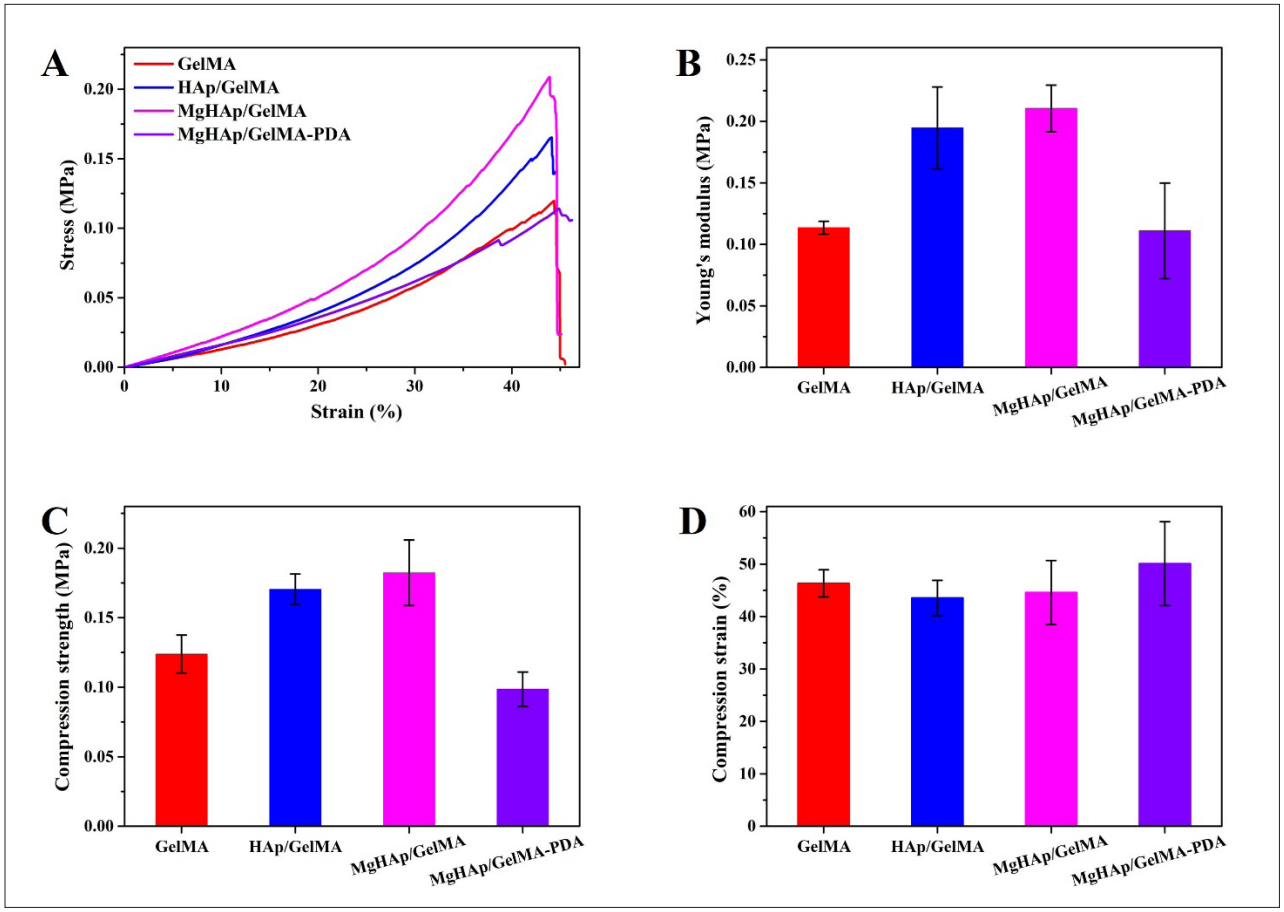

Figure 7. Mechanical properties of printed hydrogels in wet state. (A–D) Typical compression stress–strain curves (A), Young's modulus (B), compression strength (C), and compression strain (D) of 3D-printed GelMA, HAp/GelMA, MgHAp/GelMA, and MgHAp/GelMA-PDA hydrogels.

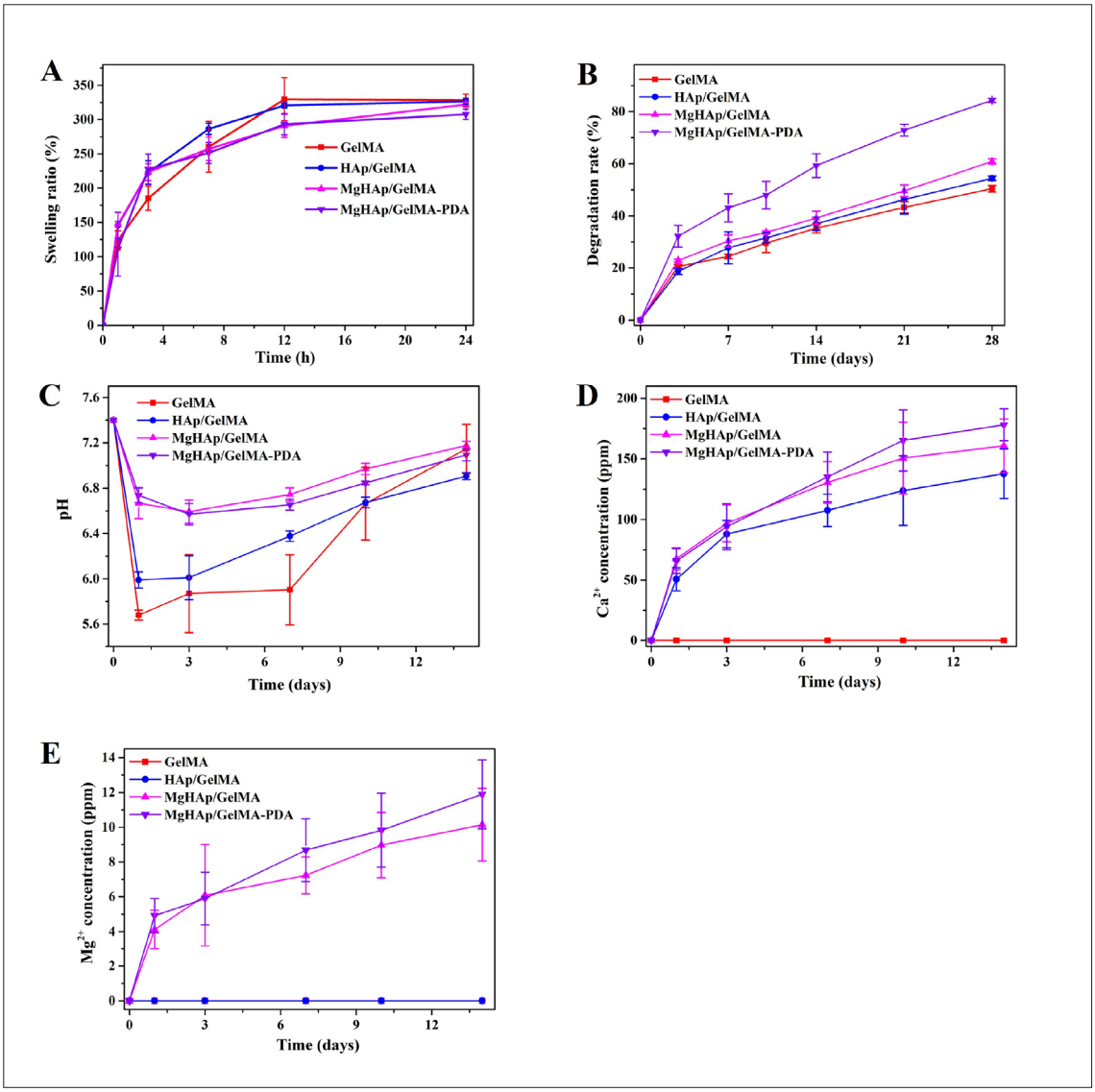

Figure 8. Swelling behavior (A), *in vitro* degradation behavior (B), pH change (C), Ca^{2+} release (D), and Mg^{2+} release (E) of 3D-printed GelMA, HAp/GelMA, MgHAp/GelMA, and MgHAp/GelMA-PDA hydrogels.

DOX was released from the hydrogels under NIR laser irradiation (Figure 9D). Additionally, a higher power density of NIR laser elicited a larger release of DOX. The NIR laser irradiation greatly promoted DOX release from MgHAp/GelMA-PDA@DOX hydrogels, which was possibly due to the Brownian movements of molecules. The entropy and temperature of MgHAp/GelMA-PDA@DOX hydrogels was enhanced when heated by NIR laser irradiation, thereby accelerating the movements of DOX molecules and the disintegration of hydrogels.

Since the tumor microenvironment is often acidic and hypoxic, studying DOX release in buffer solutions with different pH values (pH 4.5 and 7.4) is essential. As shown in Figures 9E and S6, Supporting Information, compared to PDA@DOX particles in which DOX could be quickly released in 12 h in either PBS or acidic solution, DOX could be sustainably released from MgHAp/GelMA-PDA@DOX hydrogels for more than 7 days in an acidic environment while the release of DOX reached a plateau after 3 days being immersed in PBS at pH 7.4. The sustained DOX release in acidic environment would achieve a prolonged therapeutic effect and hence could facilitate cell membrane permeability and effectively kill tumor cells.[64]

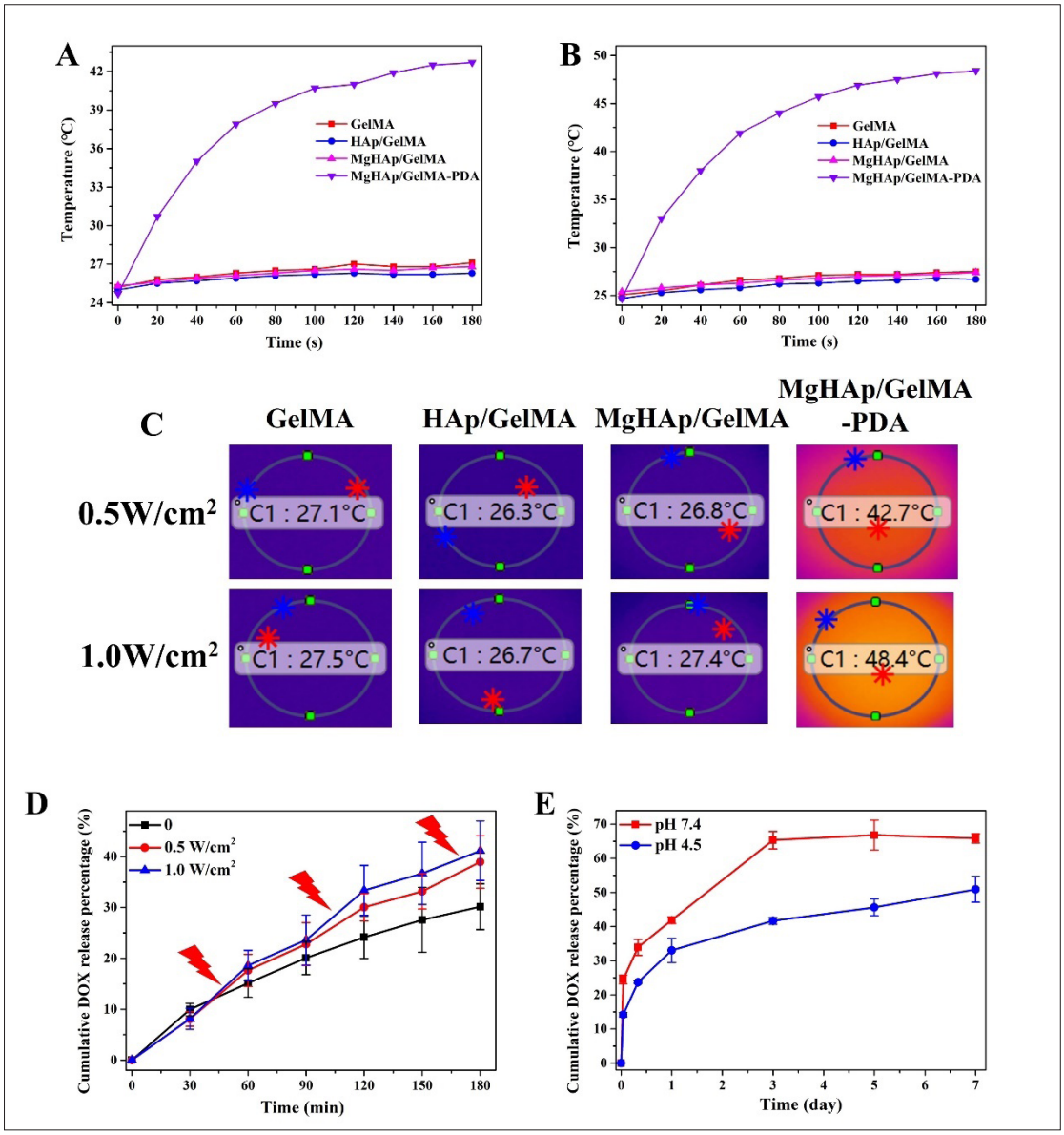

Figure 9. Photothermal effect and controlled DOX release behavior of printed hydrogels. (A, B) Temperature changes of 3D-printed GelMA, HAp/GelMA, MgHAp/GelMA, and MgHAp/GelMA-PDA hydrogels under the irradiation of 808 nm NIR laser at power densities of 0.5 W/cm^2 (A) and 1.0 W/cm^2 (B). (C) Infrared thermal images of 3D-printed GelMA, HAp/GelMA, MgHAp/GelMA, and MgHAp/GelMA-PDA hydrogels after being irradiated by NIR laser for 3 min. (D) *In vitro* DOX release curves of MgHAp/GelMA-PDA@DOX hydrogels with (0.5 and 1.0 W/cm^2) and without NIR laser irradiation (pH 7.4, PBS). (E) *In vitro* DOX release curves of MgHAp/GelMA-PDA@DOX hydrogels in pH 4.5 and 7.4 buffer solutions.

3.5. *In vitro* antitumor efficiency

Chemotherapy assisted by PTT enables the controlled release of DOX on demand while simultaneously providing hyperthermia, showing great synergy for tumor treatment. Many studies have revealed that NIR laser irradiation could cause the local temperature within the range of 42–50°C and thus provide hyperthermia and synergistically stimulate DOX release to improve anticancer therapy.[4,9,65] Therefore, in the current study, 3D-printed MgHAp/GelMA-PDA@DOX hydrogels combined with NIR laser irradiation were employed to investigate the *in vitro* antitumor efficiency. As shown in Figure 10A, after being cultured for 4 and 24 h, many bone tumor cells were found dead in the MgHAp/GelMA-PDA+NIR, MgHAp/GelMA-PDA@DOX, and MgHAp/GelMA-PDA@DOX+NIR groups. Moreover, Figure 10B indicates that the cell survival rates of MG63 cells in the MgHAp/GelMA-PDA, MgHAp/GelMA-PDA+NIR, MgHAp/GelMA-PDA@DOX, and

MgHAp/GelMA-PDA@DOX+NIR groups, after being cultured for 24 h, were 96.66 ± 0.11%, 47.01 ± 0.93%, 42.57 ± 3.11%, and 8.53 ± 1.12 %, respectively. Compared to the MgHAp/GelMA-PDA group, the MgHAp/GelMA-PDA+NIR and MgHAp/GelMA-PDA@DOX groups exhibited dramatically lower cell survival rates, which could be attributed to the hyperthermia triggered by NIR laser irradiation or the sustained release of DOX. Additionally, almost all MG63 cells were eradicated in the MgHAp/GelMA-PDA@DOX+NIR group after 24 h of culture, as a result of the synergistic effect of chemotherapy and hyperthermia induced by NIR laser. The significant decrease in cell viability of MG63 cells in the MgHAp/GelMA-PDA@DOX+NIR group further confirmed the synergistic effect of chemotherapy and PTT for tumor cell eradication (Figure 10C). Consequently, 3D-printed MgHAp/GelMA-PDA@DOX hydrogels that had been irradiated by NIR laser possessed excellent antitumor efficiency and could decimate tumor cells through the synergy of chemotherapy and PTT.

3.6. Proliferation and osteogenic differentiation of 3D-printed hydrogels

To investigate the *in vitro* biological properties of printed hydrogels, rBMSCs were cultured on the hydrogels. It is well-known that GelMA contains RGD sequences that can promote cell attachment and growth. As shown in Figure 11, all 3D-printed hydrogels were conducive to cell growth. In the current study, HAp/GelMA hydrogels exhibited a higher proliferation rate of rBMSCs than GelMA hydrogels. This could be attributed to the enhanced mechanical strength of hydrogels due to the incorporation of HAp nanocomposites. Meanwhile, compared to HAp/GelMA hydrogels, MgHAp/GelMA hydrogels exhibited a higher proliferation rate of rBMSCs, which could result from the release of Mg^{2+}. Previous studies showed that Mg^{2+} could enhance cell attachment and proliferation.[35,66] Notably, because of the encapsulation of PDA particles, MgHAp/GelMA-PDA hydrogels exhibited the highest cell proliferation rate. Many studies have reported that PDA particles could facilitate cell adhesion and proliferation.[67]

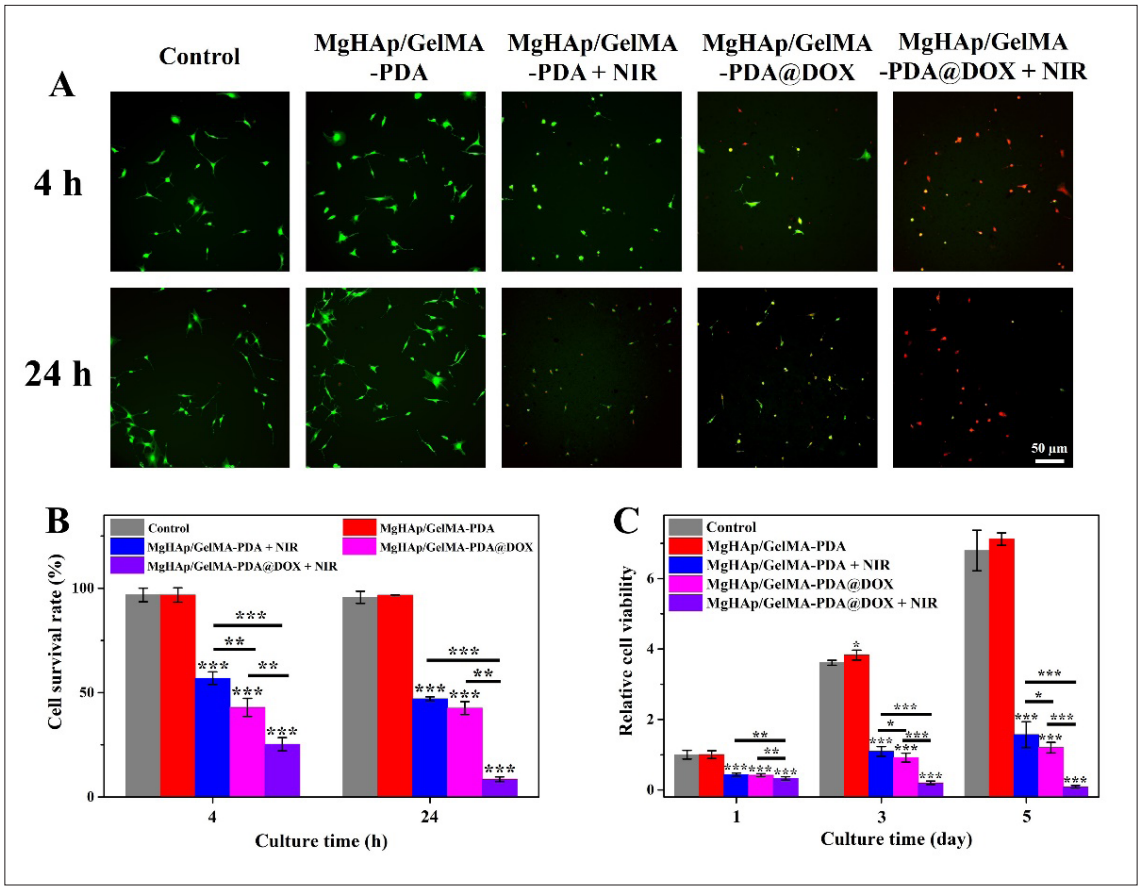

Figure 10. *In vitro* antitumor efficiency of MgHAp/GelMA-PDA@DOX hydrogels irradiated by NIR laser. (A) Fluorescence images showing the morphology of living and dead MG63 cells incubated on hydrogels for 4 and 24 h. (B) Cell survival rates of MG63 cells on hydrogels after incubation for 4 and 24 h. (C) Relative cell viability of MG63 cells cultured on hydrogels for 1, 3, and 5 days.

For example, Yang et al. suggested that PDA particles possessed a large amount of amine and hydroxyl groups and thus benefited cell adhesion, spread, and growth.[68]

To investigate the osteogenic effect of printed hydrogels, the ALP activity expression was studied. As shown in Figure 12A and B, the ALP activity of rBMSCs on HAp/GelMA hydrogels was higher than that on GelMA hydrogels. Previous studies have demonstrated that HAp nanocomposites could promote the osteogenic differentiation of rBMSCs.[69,70] Moreover, MgHAp/GelMA and MgHAp/GelMA-PDA hydrogels exhibited the highest ALP activity expression after 7 and 14 days of culture, showing good osteogenic effect. Furthermore, the qRT-PCR results, as shown in Figure 12C–F, indicated that the expression of osteogenic genes, *i.e.*, *Ocn*, *Col1*, *Runx2*, and *Bmp2*, in MgHAp/GelMA and MgHAp/GelMA-PDA hydrogels was upregulated in comparison to GelMA and HAp/GelMA hydrogels. The confocal images in Figure 12G further demonstrates that MgHAp/GelMA and MgHAp/GelMA-PDA hydrogels had the highest expression of COL1. As a result, the sustained release of Mg^{2+} from MgHAp/GelMA and MgHAp/GelMA-PDA hydrogels significantly promoted osteogenic differentiation of rBMSCs, which was consistent with previous studies.[36,71,72] Mg^{2+} could regulate osteoblast activity by binding to the specific sites on the integrin α chains of cell surface and thus promote the expression of osteogenic genes. For example, Sun et al. showed that Mg^{2+} released from Wollastonite ceramic could promote the ALP activity, the expression of osteogenic genes, such as *Ocn*, *Runx2*, *Col1*, and *Osx* of MC3T3-E1 cells, and the repair of rabbit skull defects.[73] As a result, 3D-printed MgHAp/GelMA-PDA@DOX hydrogels showed great potential for treating bone tumor-related defects by providing synergy for effectively eradicating tumor cells and promoting osteogenesis.

4. Conclusion

In the current study, MgHAp nanocomposites were synthesized via a biomineralization process. GelMA and PDA@DOX particles were fabricated. MgHAp/GelMA-PDA@DOX hydrogels were constructed via 3D printing. MgHAp nanocomposites and PDA particles

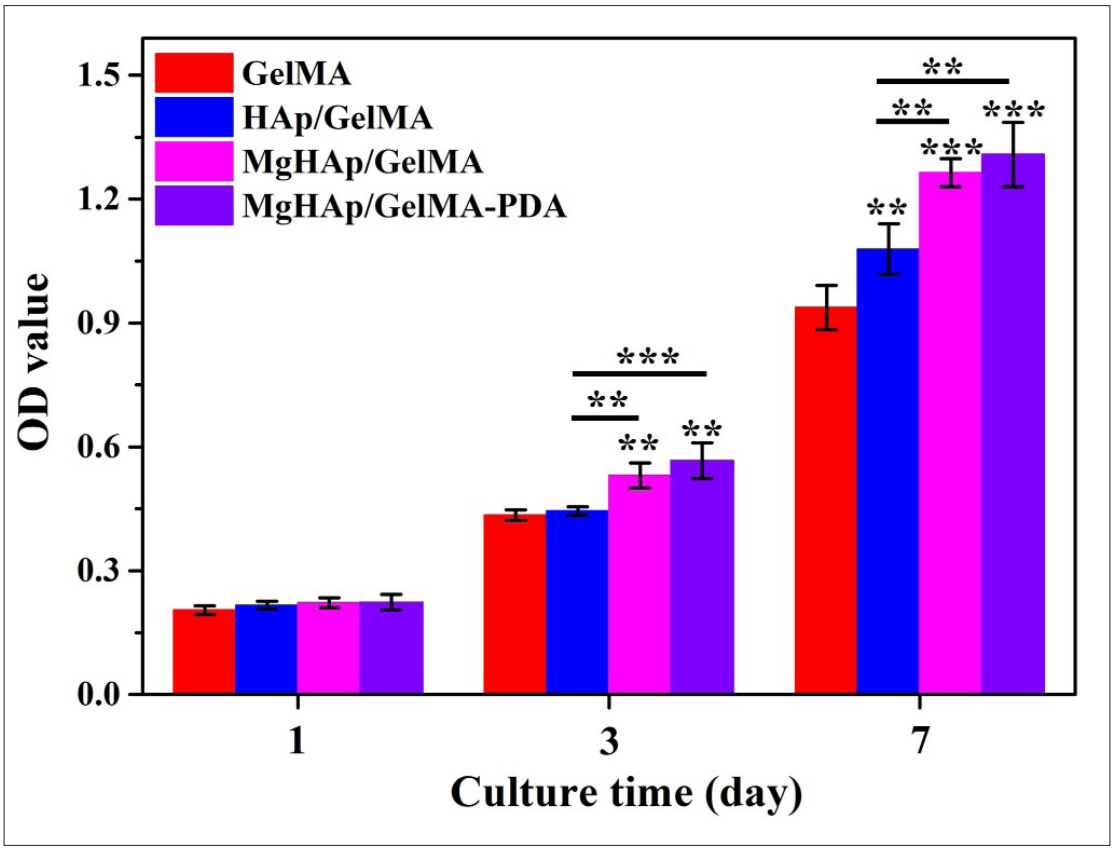

Figure 11. Proliferation profiles of rBMSCs cultured on 3D-printed GelMA, HAp/GelMA, MgHAp/GelMA, and MgHAp/GelMA-PDA hydrogels. ** $p < 0.01$, *** $p < 0.001$ versus GelMA.

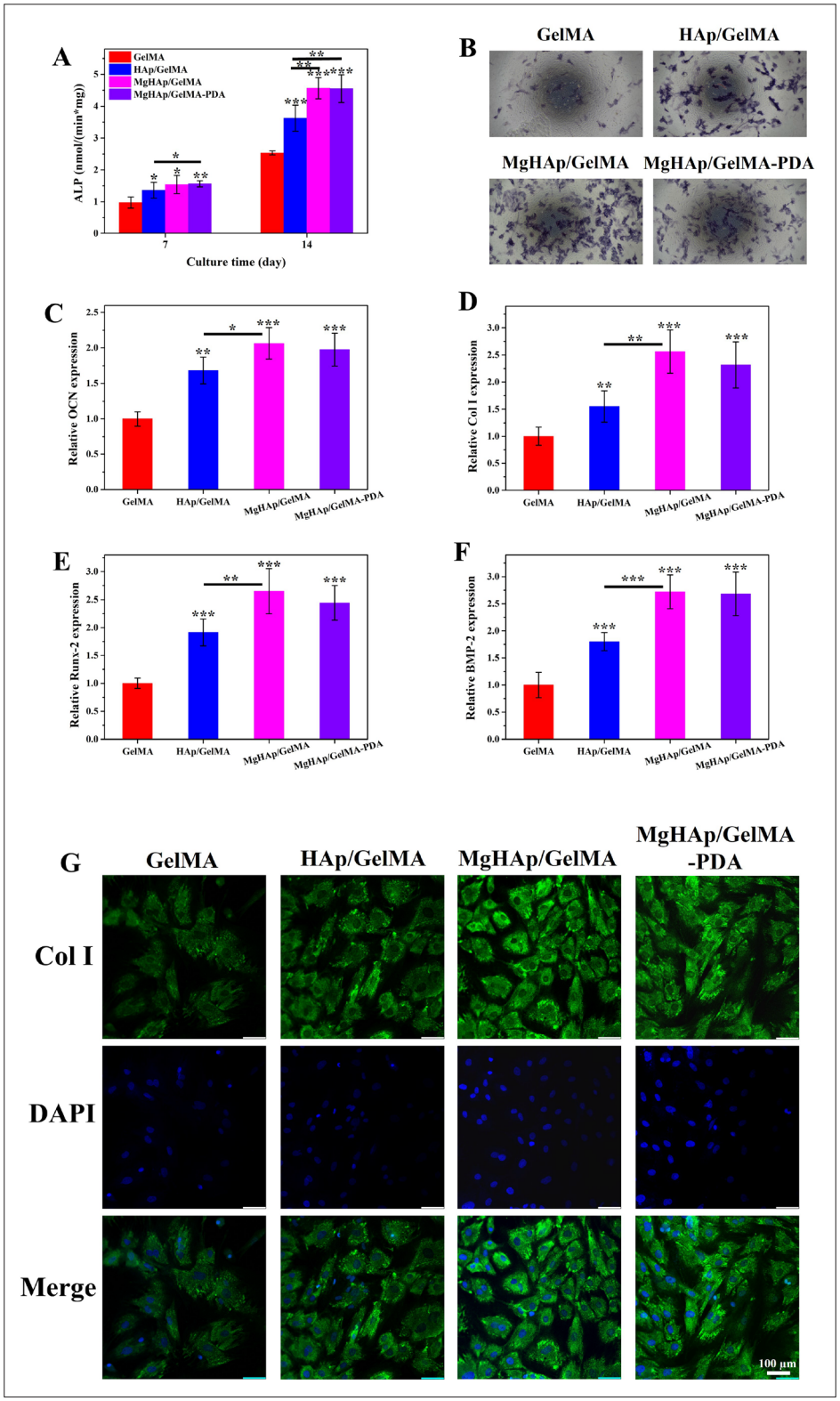

Figure 12. Osteogenic differentiation of rBMSCs on hydrogels. (A) Alkaline phosphatase (ALP) activity of rBMSCs on hydrogels after being cultured for 7 and 14 days. (B) Optical images showing the ALP staining results of rBMSCs cultured for 14 days. (C–F) The relative expression of osteogenic genes, namely *Ocn* (C), *Col1* (D), *Runx2* (E), and *Bmp2* (F), in rBMSCs cultured on hydrogels for 14 days. (G) Confocal images showing the expression of COL1 in rBMSCs cultured on hydrogels for 14 days.

were homogenously dispersed within the hydrogels. The incorporation of MgHAp nanocomposites improved the printability of inks and promoted structural fidelity of printed structures. Additionally, MgHAp nanocomposites enhanced the mechanical strength of hydrogels. Moreover, MgHAp/GelMA-PDA@DOX hydrogels enabled the sustained and controlled release of Mg^{2+}. MgHAp/GelMA-PDA@DOX hydrogels exhibited an excellent photothermal effect and could generate hyperthermia upon irradiation with NIR laser. The release of DOX from hydrogels could be controlled by NIR laser irradiation and was also pH-responsive. *In vitro* antitumor experiments indicated that MgHAp/GelMA-PDA@DOX hydrogels could effectively kill the MG63 osteosarcoma cells through the synergistic effect of induced hyperthermia and DOX release. Moreover, compared to HAp/GelMA hydrogels, MgHAp/GelMA-PDA hydrogels could promote proliferation and osteogenic differentiation of rBMSCs due to the sustained release of Mg^{2+}. Consequently, 3D-printed MgHAp/GelMA-PDA@DOX hydrogels hold great promise in treating bone tumor-related defects by providing effective anti-tumor efficiency and the promotion of osteogenic effect.

Acknowledgments

None

Funding

This work was financially supported by the National Nature Science Foundation of China (Grant No. 82201133) and Fong On Construction Ltd. in Hong Kong (Grant No. ZDBM, ZDCA). The research sponsored from Fong On Construction Ltd. (HK) has potential interest in exploring the potential application of extrusion-based 3D printing technology in automation within the construction industry.

Conflict of interest

The authors declare no conflicts of interest.

Author contributions

Conceptualization: Shangsi Chen, Shenglong Tan
Investigation: Shangsi Chen, Yue Wang, Junzhi Li
Methodology: Shangsi Chen, Yue Wang, Junzhi Li
Supervision: Haoran Sun, Ming-Fung Francis Siu, Shenglong Tan
Writing – original draft: All authors
Writing – review & editing: Haoran Sun, Ming-Fung Francis Siu, Shenglong Tan

Ethics approval and consent to participate

Not applicable.

Consent for publication

Not applicable.

Availability of data

Data are available from the corresponding author upon reasonable request.

References

1. Isakoff MS, Bielack SS, Meltzer P, Gorlick R. Osteosarcoma: current treatment and a collaborative pathway to success. *J Clin Oncol*. 2015;33(27):3029-3035. doi: 10.1200/JCO.2014.59.4895
2. Chen HHW, Kuo MT. Improving radiotherapy in cancer treatment: promises and challenges. *Oncotarget*. 2017;8(37):62742-62758. doi: 10.18632/oncotarget.18409
3. Behranvand N, Nasri F, Zolfaghari Emameh R, et al. Chemotherapy: a double-edged sword in cancer treatment. *Cancer Immunol Immunother*. 2022;71(3):507-526. doi: 10.1007/s00262-021-03013-3
4. Su J, Sun H, Meng Q, et al. Bioinspired nanoparticles with NIR-controlled drug release for synergetic chemophotothermal therapy of metastatic breast cancer. *Adv Funct Mater*. 2016;26(41):7495-7506. doi: 10.1002/adfm.201603381
5. Fan R, Chen C, Hou H, et al. Tumor acidity and near-infrared light responsive dual drug delivery polydopamine-based nanoparticles for chemo-photothermal therapy. *Adv Funct Mater*. 2021;31(18):2009733. doi: 10.1002/adfm.202009733
6. An D, Fu J, Zhang B, et al. NIR-II responsive inorganic 2D nanomaterials for cancer photothermal therapy: recent advances and future challenges. *Adv Funct Mater*. 2021;31(32):2101625. doi: 10.1002/adfm.202101625
7. Ren Y, Yan Y, Qi H. Photothermal conversion and transfer in photothermal therapy: from macroscale to nanoscale. *Adv Colloid Interface Sci*. 2022;308:102753. doi: 10.1016/j.cis.2022.102753
8. Batul R, Tamanna T, Khaliq A, Yu A. Recent progress in the biomedical applications of polydopamine nanostructures. *Biomater Sci*. 2017;5(7):1204-1229. doi: 10.1039/c7bm00187h
9. Qiu J, Shi Y, Xia Y. Polydopamine nanobottles with photothermal capability for controlled release and related applications. *Adv Mater*. 2021;33(45):e2104729. doi: 10.1002/adma.202104729
10. Bedhiafi T, Idoudi S, Alhams AA, et al. Applications of polydopaminic nanomaterials in mucosal drug delivery. *J Control Release*. 2023;353:842-849.

doi: 10.1016/j.jconrel.2022.12.037

11. Chen S, Tan S, Zheng L, Wang M. Multilayered shape-morphing scaffolds with a hierarchical structure for uterine tissue regeneration. *ACS Appl Mater Interfaces*. 2024;16(6):6772-6788.
doi: 10.1021/acsami.3c14983

12. Abbasi N, Hamlet S, Love RM, Nguyen NT. Porous scaffolds for bone regeneration. *J Sci: Adv Mater Devices*. 2020; 5(1):1-9.
doi: 10.1016/j.jsamd.2020.01.007

13. Chen S, Shi Y, Zhang X, Ma J. Evaluation of BMP-2 and VEGF loaded 3D printed hydroxyapatite composite scaffolds with enhanced osteogenic capacity in vitro and in vivo. *Mater Sci Eng C Mater Biol Appl*. 2020;112:110893.
doi: 10.1016/j.msec.2020.110893

14. Bose S, Roy M, Bandyopadhyay A. Recent advances in bone tissue engineering scaffolds. *Trends Biotechnol*. 2012;30(10):546-554.
doi: 10.1016/j.tibtech.2012.07.005

15. Roseti L, Parisi V, Petretta M, et al. Scaffolds for bone tissue engineering: state of the art and new perspectives. *Mater Sci Eng C Mater Biol Appl*. 2017;78:1246-1262.
doi: 10.1016/j.msec.2017.05.017

16. Lai J, Wang C, Liu J, et al. Low temperature hybrid 3D printing of hierarchically porous bone tissue engineering scaffolds within situdelivery of osteogenic peptide and mesenchymal stem cells. *Biofabrication*. 2022;14(4):045006.
doi: 10.1088/1758-5090/ac84b0

17. Do AV, Khorsand B, Geary SM, Salem AK. 3D printing of scaffolds for tissue regeneration applications. *Adv Healthc Mater*. 2015;4(12):1742-1762.
doi: 10.1002/adhm.201500168

18. Wang S, Zhao S, Yu J, Gu Z, Zhang Y. Advances in translational 3D printing for cartilage, bone, and osteochondral tissue engineering. *Small*. 2022;18(36):e2201869.
doi: 10.1002/smll.202201869

19. MacDonald E, Wicker R. Multiprocess 3D printing for increasing component functionality. *Science*. 2016;353(6307):aaf2093.
doi: 10.1126/science.aaf2093

20. Velasquez-Garcia LF, Kornbluth Y. Biomedical applications of metal 3D printing. *Annu Rev Biomed Eng*. 2021;23: 307-338.
doi: 10.1146/annurev-bioeng-082020-032402

21. Ratheesh G, Vaquette C, Xiao Y. Patient-specific bone particles bioprinting for bone tissue engineering. *Adv Healthc Mater*. 2020;9(23):e2001323.
doi: 10.1002/adhm.202001323

22. Van hede D, Liang B, Anania S, et al. 3D-printed synthetic hydroxyapatite scaffold with in silico optimized macrostructure enhances bone formation in vivo. *Adv Funct Mater*. 2021;32(6):2105002.
doi: 10.1002/adfm.202105002

23. Wang Y, Chen SS, Liang HW, Liu Y, Bai JM, Wang M. Digital light processing (DLP) of nano biphasic calcium phosphate bioceramic for making bone tissue engineering scaffolds. *Ceram Int*. 2022;48(19):27681-27692.
doi: 10.1016/j.ceramint.2022.06.067

24. Yin J, Yan M, Wang Y, Fu J, Suo H. 3D bioprinting of low-concentration cell-laden gelatin methacrylate (GelMA) bioinks with a two-step cross-linking strategy. *ACS Appl Mater Interfaces*. 2018;10(8):6849-6857.
doi: 10.1021/acsami.7b16059

25. Guo A, Zhang S, Yang R, Sui C. Enhancing the mechanical strength of 3D printed GelMA for soft tissue engineering applications. *Mater Today Bio*. 2024; 24:100939.
doi: 10.1016/j.mtbio.2023.100939

26. Chen S, Wang Y, Lai J, Tan S, Wang M. Structure and properties of gelatin methacryloyl (GelMA) synthesized in different reaction systems. *Biomacromolecules*. 2023;24(6):2928-2941.
doi: 10.1021/acs.biomac.3c00302

27. Jiang G, Li S, Yu K, et al. A 3D-printed PRP-GelMA hydrogel promotes osteochondral regeneration through M2 macrophage polarization in a rabbit model. *Acta Biomater*. 2021;128:150-162.
doi: 10.1016/j.actbio.2021.04.010

28. Xu C, Chang Y, Xu Y, et al. Silicon-phosphorus-nanosheets-integrated 3D-printable hydrogel as a bioactive and biodegradable scaffold for vascularized bone regeneration. *Adv Healthc Mater*. 2022;11(6):e2101911.
doi: 10.1002/adhm.202101911

29. Zhang X, Zhang H, Zhang Y, et al. 3D printed reduced graphene oxide-GelMA hybrid hydrogel scaffolds for potential neuralized bone regeneration. *J Mater Chem B*. 2023;11(6):1288-1301.
doi: 10.1039/d2tb01979e

30. Xavier Mendes A, Moraes Silva S, O'Connell CD, et al. Enhanced electroactivity, mechanical properties, and printability through the addition of graphene oxide to photo-cross-linkable gelatin methacryloyl hydrogel. *ACS Biomater Sci Eng*. 2021;7(6):2279-2295.
doi: 10.1021/acsbiomaterials.0c01734

31. Choi E, Kim D, Kang D, et al. 3D-printed gelatin methacrylate (GelMA)/silanated silica scaffold assisted by two-stage cooling system for hard tissue regeneration. *Regen Biomater*. 2021;8(2):rbab001.
doi: 10.1093/rb/rbab001

32. Gui XY, Zhang BQ, Song P, et al. 3D printing of biomimetic hierarchical porous architecture scaffold with dual osteoinduction and osteoconduction biofunctions for large size bone defect repair. *Appl Mater Today*. 2024; 37:102085.
doi: 10.1016/j.apmt.2024.102085

33. Pu X, Tong L, Wang X, et al. Bioinspired hydrogel anchoring 3DP GelMA/HAp scaffolds accelerates bone reconstruction. *ACS Appl Mater Interfaces*. 2022;14(18):20591-20602. doi: 10.1021/acsami.1c25015

34. Song P, Li MX, Zhang BQ, et al. DLP fabricating of precision GelMA/HAp porous composite scaffold for bone tissue engineering application. *Compos B Eng*. 2022;244:110163. doi: 10.1016/j.compositesb.2022.110163

35. Chen S, Shi Y, Zhang X, Ma J. Biomimetic synthesis of Mg-substituted hydroxyapatite nanocomposites and three-dimensional printing of composite scaffolds for bone regeneration. *J Biomed Mater Res A*. 2019;107(11): 2512-2521. doi: 10.1002/jbm.a.36757

36. Zhou H, Liang B, Jiang HT, Deng ZL, Yu KX. Magnesium-based biomaterials as emerging agents for bone repair and regeneration: from mechanism to application. *J Magnes Alloy*. 2021;9(3):779-804. doi: 10.1016/j.jma.2021.03.004

37. Chen S, Wang Y, Zhang X, Ma J, Wang M. Double-crosslinked bifunctional hydrogels with encapsulated anti-cancer drug for bone tumor cell ablation and bone tissue regeneration. *Colloids Surf B Biointerfaces*. 2022;213:112364. doi: 10.1016/j.colsurfb.2022.112364

38. Ouyang L, Yao R, Zhao Y, Sun W. Effect of bioink properties on printability and cell viability for 3D bioplotting of embryonic stem cells. *Biofabrication*. 2016;8(3):035020. doi: 10.1088/1758-5090/8/3/035020

39. Ma J, Wang J, Ai X, Zhang S. Biomimetic self-assembly of apatite hybrid materials: from a single molecular template to bi-/multi-molecular templates. *Biotechnol Adv*. 2014;32(4):744-60. doi: 10.1016/j.biotechadv.2013.10.014

40. Luo Y, Chen S, Shi Y, Ma J. 3D printing of strontium-doped hydroxyapatite based composite scaffolds for repairing critical-sized rabbit calvarial defects. *Biomed Mater*. 2018;13(6):065004. doi: 10.1088/1748-605X/aad923

41. Kang Y, Xu C, Meng L, Dong X, Qi M, Jiang D. Exosome-functionalized magnesium-organic framework-based scaffolds with osteogenic, angiogenic and anti-inflammatory properties for accelerated bone regeneration. *Bioact Mater*. 2022;18:26-41. doi: 10.1016/j.bioactmat.2022.02.012

42. Antoniac IV, Antoniac A, Vasile E, et al. In vitro characterization of novel nanostructured collagen-hydroxyapatite composite scaffolds doped with magnesium with improved biodegradation rate for hard tissue regeneration. *Bioact Mater*. 2021;6(10):3383-3395. doi: 10.1016/j.bioactmat.2021.02.030

43. Chen SS, Li JZ, Zheng LW, Huang J, Wang M. Biomimicking trilayer scaffolds with controlled estradiol release for uterine tissue regeneration. *Exploration*. 2024:20230141. doi: 10.1002/Exp.20230141

44. Kumar H, Sakthivel K, Mohamed MGA, Boras E, Shin SR, Kim K. Designing gelatin methacryloyl (GelMA)-based bioinks for visible light stereolithographic 3D biofabrication. *Macromol Biosci*. 2021;21(1):e2000317. doi: 10.1002/mabi.202000317

45. Lee BH, Lum N, Seow LY, Lim PQ, Tan LP. Synthesis and characterization of types A and B gelatin methacryloyl for bioink applications. *Materials (Basel)*. 2016;9(10):797. doi: 10.3390/ma9100797

46. Wang Z, Duan Y, Duan Y. Application of polydopamine in tumor targeted drug delivery system and its drug release behavior. *J Control Release*. 2018;290:56-74. doi: 10.1016/j.jconrel.2018.10.009

47. Yue K, Trujillo-de Santiago G, Alvarez MM, Tamayol A, Annabi N, Khademhosseini A. Synthesis, properties, and biomedical applications of gelatin methacryloyl (GelMA) hydrogels. *Biomaterials*. 2015;73:254-271. doi: 10.1016/j.biomaterials.2015.08.045

48. Outrequin TCR, Gamonpilas C, Siriwatwechakul W, Sreearunothai P. Extrusion-based 3D printing of food biopolymers: a highlight on the important rheological parameters to reach printability. *J Food Eng*. 2023; 342:111371. doi: 10.1016/j.jfoodeng.2022.111371

49. Sanchez-Sanchez R, Rodriguez-Rego JM, Macias-Garcia A, Mendoza-Cerezo L, Diaz-Parralejo A. Relationship between shear-thinning rheological properties of bioinks and bioprinting parameters. *Int J Bioprint*. 2023; 9(2):687. doi: 10.18063/ijb.687

50. Kyle S, Jessop ZM, Al-Sabah A, Whitaker IS. 'Printability' of candidate biomaterials for extrusion based 3D printing: state-of-the-art. *Adv Healthc Mater*. 2017;6(16):1700264. doi: 10.1002/adhm.201700264

51. Schwab A, Levato R, D'Este M, Piluso S, Eglin D, Malda J. Printability and shape fidelity of bioinks in 3D bioprinting. *Chem Rev*. 2020;120(19):11028-11055. doi: 10.1021/acs.chemrev.0c00084

52. Ning L, Mehta R, Cao C, et al. Embedded 3D bioprinting of gelatin methacryloyl-based constructs with highly tunable structural fidelity. *ACS Appl Mater Interfaces*. 2020;12(40):44563-44577. doi: 10.1021/acsami.0c15078

53. Mora-Boza A, Wlodarczyk-Biegun MK, Del Campo A, Vazquez-Lasa B, Roman JS. Glycerylphytate as an ionic crosslinker for 3D printing of multi-layered scaffolds with improved shape fidelity and biological features. *Biomater Sci*. 2019;8(1):506-516. doi: 10.1039/c9bm01271k

54. Latif M, Jiang Y, Kumar B, Song JM, Cho HC, Kim J. High content nanocellulose 3D-printed and esterified structures with strong interfacial adhesion, high mechanical

properties, and shape fidelity. *Adv Mater Interfaces*. 2022;9(16):202200280.
doi: 10.1002/admi.202200280

55. Bose S, Vahabzadeh S, Bandyopadhyay A. Bone tissue engineering using 3D printing. *Mater Today*. 2013;16(12):496-504.
doi: 10.1016/j.mattod.2013.11.017

56. Wang ZC, Huang CZ, Han X, et al. Fabrication of aerogel scaffolds with adjustable macro/micro-pore structure through 3D printing and sacrificial template method for tissue engineering. *Mater Design*. 2022;217(1):110662.
doi: 10.1016/j.matdes.2022.110662

57. Rizwan M, Chan SW, Comeau PA, Willett TL, Yim EKF. Effect of sterilization treatment on mechanical properties, biodegradation, bioactivity and printability of GelMA hydrogels. *Biomed Mater*. 2020;15(6):065017.
doi: 10.1088/1748-605X/aba40c

58. O'Connell CD, Zhang B, Onofrillo C, et al. Tailoring the mechanical properties of gelatin methacryloyl hydrogels through manipulation of the photocrosslinking conditions. *Soft Matter*. 2018;14(11):2142-2151.
doi: 10.1039/c7sm02187a

59. Bashir S, Hina M, Iqbal J, et al. Fundamental concepts of hydrogels: synthesis, properties, and their applications. *Polymers (Basel)*. 2020;12(11):2702.
doi: 10.3390/polym12112702

60. Piao Y, You H, Xu T, et al. Biomedical applications of gelatin methacryloyl hydrogels. *Eng Regen*. 2021;2:47-56.
doi: 10.1016/j.engreg.2021.03.002

61. Zhang XA, Wei H, Dong C, et al. 3D printed hydrogel/bioceramics core/shell scaffold with NIR-II triggered drug release for chemo-photothermal therapy of bone tumors and enhanced bone repair. *Chem Eng J*. 2023; 461:141855.
doi: 10.1016/j.cej.2023.141855

62. Jin A, Wang Y, Lin K, Jiang L. Nanoparticles modified by polydopamine: working as "drug" carriers. *Bioact Mater*. 2020;5(3):522-541.
doi: 10.1016/j.bioactmat.2020.04.003

63. Cheng W, Nie JP, Gao NS, et al. A multifunctional nanoplatform against multidrug resistant cancer: merging the best of targeted chemo/gene/photothermal therapy. *Adv Funct Mater*. 2017;27(45):1704135.
doi: 10.1002/adfm.201704135

64. Shahzadi I, Islam M, Saeed H, et al. Formation of biocompatible MgO/cellulose grafted hydrogel for efficient bactericidal and controlled release of doxorubicin. *Int J Biol Macromol*. 2022;220:1277-1286.
doi: 10.1016/j.ijbiomac.2022.08.142

65. Chu X, Zhang L, Li Y, He Y, Zhang Y, Du C. NIR responsive doxorubicin-loaded hollow copper ferrite @ polydopamine for dynergistic chemodynamic/photothermal/chemo-therapy. *Small*. 2023;19(7):e2205414.
doi: 10.1002/smll.202205414

66. Gao P, Fan B, Yu X, et al. Biofunctional magnesium coated Ti6Al4V scaffold enhances osteogenesis and angiogenesis in vitro and in vivo for orthopedic application. *Bioact Mater*. 2020;5(3):680-693.
doi: 10.1016/j.bioactmat.2020.04.019

67. Qian Y, Zhao X, Han Q, Chen W, Li H, Yuan W. An integrated multi-layer 3D-fabrication of PDA/RGD coated graphene loaded PCL nanoscaffold for peripheral nerve restoration. *Nat Commun*. 2018;9(1):323.
doi: 10.1038/s41467-017-02598-7

68. Yang Z, Si J, Cui Z, et al. Biomimetic composite scaffolds based on surface modification of polydopamine on electrospun poly(lactic acid)/cellulose nanofibrils. *Carbohydr Polym*. 2017;174:750-759.
doi: 10.1016/j.carbpol.2017.07.010

69. Cheng H, Chabok R, Guan X, et al. Synergistic interplay between the two major bone minerals, hydroxyapatite and whitlockite nanoparticles, for osteogenic differentiation of mesenchymal stem cells. *Acta Biomater*. 2018;69:342-351.
doi: 10.1016/j.actbio.2018.01.016

70. Liu X, Wei Y, Xuan C, et al. A biomimetic biphasic osteochondral scaffold with layer-specific release of stem cell differentiation inducers for the reconstruction of osteochondral defects. *Adv Healthc Mater*. 2020;9(23):e2000076.
doi: 10.1002/adhm.202000076

71. Li D, Zhang D, Yuan Q, et al. In vitro and in vivo assessment of the effect of biodegradable magnesium alloys on osteogenesis. *Acta Biomater*. 2022;141:454-465.
doi: 10.1016/j.actbio.2021.12.032

72. Wang L, Pang Y, Tang Y, et al. A biomimetic piezoelectric scaffold with sustained Mg(2+) release promotes neurogenic and angiogenic differentiation for enhanced bone regeneration. *Bioact Mater*. 2023;25:399-414.
doi: 10.1016/j.bioactmat.2022.11.004

73. Sun M, Liu A, Shao H, et al. Systematical evaluation of mechanically strong 3D printed diluted magnesium doping wollastonite scaffolds on osteogenic capacity in rabbit calvarial defects. *Sci Rep*. 2016;6:34029.
doi: 10.1038/srep34029